University of Glasgow
DEPARTMENT OF
AEROSPACE
ENGINEERING

A CFD INVESTIGATION INTO THE MODIFICATION OF A UAV AIRFRAME

Martin Millar, Ladislav Smrcek

Report No. 0109

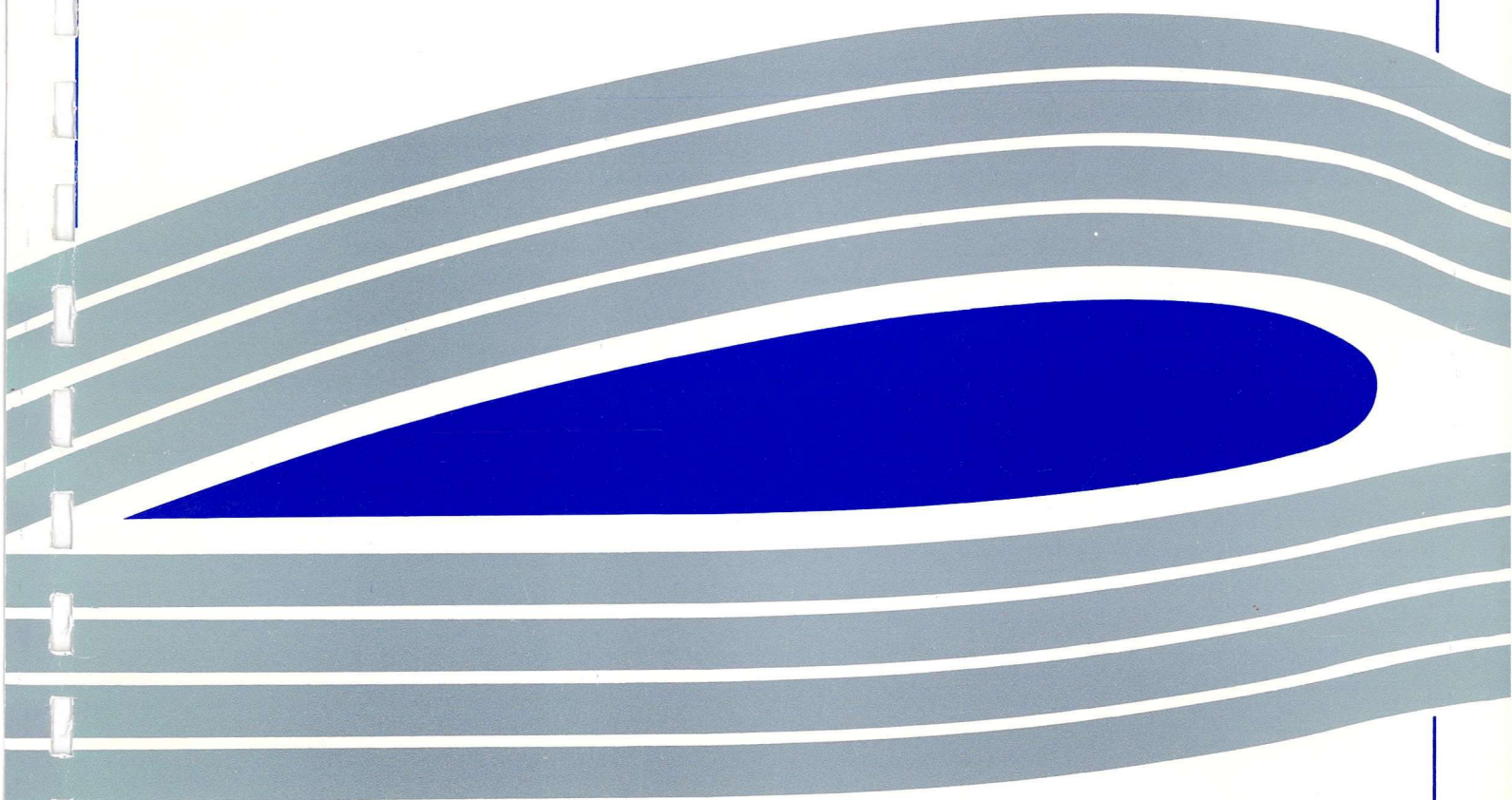

A CFD INVESTIGATION INTO THE MODIFICATION OF A UAV AIRFRAME

Martin Millar, Ladislav Smrcek
Report No. 0109

CONTENTS

1. ABSTRACT

A computational analysis was undertaken at the Czech Aeronautical Test and Research Institute (ARTI) on the outskirts of Prague into the possibility of implementing a new design of Unmanned Aerial Vehicle (UAV) for the Czech military.

The analysis was carried out using a compendium of programs used in the design of streamlined bodies. CMARC was the name of the analysing program, which is just a simple panel method and also undertakes inviscid calculations. Prior to analysis the model surface and wake are all that require meshing.

Surface pressure coefficient plots were obtained along with lift and moment coefficients at the specific angles of attack. Drag coefficients were calculated using hand methods, also done at the ARTI, and with this data drag polars and lift curves of the various configurations were obtained.

The outcome of the investigation discovered that a design of UAV that retained the current set up, however, swapping the aerofoil and increasing the span slightly provided the best performance characteristics. Though this conclusion was placed in doubt due to a number of shortcomings in the program, which had numerous limitations as in this situation it was being used as an analysis tool and not a basic design tool which is its intended function. Thus, the analysis ideally should be performed once again using a more suitable analysis package.

2. NOMENCLATURE

B_{JK} Velocity potential influence coefficient at control point of panel J due to a uniform distribution of unit source on panel K

C_{JK} Velocity potential influence coefficient at control point of panel J due to a uniform distribution of unit doublet on panel K

C_f	Local skin friction coefficient, $\frac{2\tau_w}{\rho U^2}$
C_D	Drag coefficient
C_L	Lift coefficient
C_M	Moment coefficient
C_τ	Local shear stress integral coefficient, $\frac{2}{\rho U^2 \delta}\int_0^\delta \tau \, d\xi$
C_P	Pressure coefficient
dS	Differential surface element on configuration
H	Boundary layer shape factor
$\bar{n}$	Unit normal vector to surface
N_S	Total number of surface panels
N_W	Total number of wake panels
P	An arbitrary point in space
$\bar{r}$	Vector between an arbitrary point P and a surface element dS
S	Surface of the configuration
S_∞	Imaginary surface at infinity
t	Time
U	Velocity at the outer edge of the boundary layer
u	Velocity in the boundary layer
u_τ	Friction velocity, $\sqrt{\frac{\tau_w}{\rho}}$

$\overline{V}$	Velocity vector
$\overline{V}_{\mu PK}$	Velocity influence coefficient at point P due to a uniform distribution of unit doublet on panel K.
$\overline{V}_{\sigma PK}$	Velocity influence coefficient at point P due to a uniform distribution of unit source on panel K.
W	Wake surface
α	Angle of attack
Φ	Total velocity potential
ϕ	Perturbation velocity potential
ϕ_∞	Free-stream velocity potential
μ	Doublet singularity strength per unit area
σ	Source singularity strength per unit area
ν	Kinematic viscosity
θ	Momentum thickness
δ	Boundary layer thickness
δ^*	Displacement thickness
τ	Shear stress
η	Generalised co-ordinate along streamline
ξ	Generalised co-ordinate normal to surface along streamline

Subscripts:

i	Interior region
J	Refers to panel J or its control point
K	Refers to panel K or its control point
L	Lower surface

P	Refers to velocity scan point P
U	Upper surface
∞	Free-stream conditions

3. INTRODUCTION

At present the University of Glasgow has the ownership of a Czech manufactured unmanned aerial vehicle (UAV)[1]. It is the long term goal of this project to refurbish this UAV and utilise it as a flying laboratory for research purposes, primarily as a design tool for aerofoil development.
Initially, this UAV was utilised by the Czech army. The Sojka (or "jay") III UAV system was developed in response to the army's requirements for a reconnaissance system. A range of between 60 – 100 km was required along with a maximum take-off weight of 150 kg. It was also necessary that the vehicle fly autonomously over 'difficult' terrain in bad weather, carrying a variety of opto-electronic, photographic and other user-defined payloads. A ground control station (GCS) would be operated by either the Czech air force or army. The overriding requirement though, was that the system be cost effective.

The system was designed and manufactured by the VTUL a PVO (Air Force and Air Defence Technical Institute) in Prague.
Initial research and development projects began in 1983. At this time aerial vehicles underwent a series of tests and various aerodynamic designs and concepts were evaluated in wind tunnels. Component stress was calculated and the control system was flight-tested. The final development stage ended in 1995, when the Czech army began its own field evaluation.

Since that time the UAV has demonstrated its capabilities and performed reconnaissance missions over rough terrain and in adverse conditions. Average flight times were 70 minutes, with a range of approximately 40 km. The UAV was also flying through dense clouds, transmitting enemy positions from areas of better visibility, at altitudes of 1000 m above sea level. Payload can include a black and white CCD TV camera and an infra red line scanner.

The full UAV system consists of five main elements; GCS, rocket-assisted launcher, transport container, off –road recovery vehicle and three or four aerial vehicles. Six men can deploy the system in less than 45 minutes.

A two-stroke, two-cylinder piston engine (22 Kw/6,400 rpm) powers the UAV with a pusher propeller. Landing can be done on the belly or by means of parachute deployment depending on the terrain. Its maximum take-off weight is 145 kg (excluding fuel, on-board avionics and landing system). The air vehicle itself has a wing span of 4.12 m and a length of 3.78 m. It is capable of flying for 2 hours to a ceiling of 3,000 m at a maximum speed of 200 km/h. The operational speed is approximately 180 km/h.

Inside the GCS are located 3 workstations. A commander can sit and view the captured images from the UAV on his monitor, obtain target positions and prepare his report and send it to headquarters. A pilot-operator monitors and controls the vehicle, whilst a payload-operator saves images of interest to disk or can print them off. His job also involves operating any photographic equipment present.

This report details the CFD analysis part of an investigation into several new UAV designs. The original UAV was analysed also and the results from this used as the comparison. The first design was the exact same as the original version though with a new aerofoil section, the next maintained this new aerofoil section and employed a longer wingspan. The last two configurations were conceptual designs, which also used this new aerofoil section, though veered away from the original Sojka design. The first one removing the twin tailboom design,

so typical of UAV's, lengthening the fuselage and having two tailfins. The final design incorporated a style of delta wing, whilst maintaining the tailbooms though joining the tails to form a triangular shape removing the need for separate horizontal and vertical stabilisers. Altogether this constitued 5 designs in total with 4 being new designs.
The original design of UAV has a wingspan of 4.m and an overall length of approximately 4m. The second configuration adopts these dimensions as to dos the thrid design but with an additional 0.5m on the wingspan making it 4.6m.
The first of the newer configurations was 2.2m in length with a 4.5m wingspan and the second of the new configurations was roughly 2.9m in length, again with a wingspan of 4.5m.

The analysis was undertaken at the Czech Aeronautical Test and Research Institute (ARTI), Prague as part of an ongoing research inititative between the University of Glasgow and ARTI. A series of 3 programs (Loftsman[1], CMARC[2] and Postmarc[3]) were used to analyse the configurations. The first program was used to configure the geometric values of the vehicles and to mesh them ready for the calculating program, then any results could be viewed in the final program.
It should be pointed out at this stage that the program used to calculate the parameters was inviscid, so no drag values could be obtained, these were obtained at the institute by using another program. The program can however calculate induced drag, so at low angles of attack where there is little or no separation, the results have some credence, though it is in the best interests to ignore all the drag values calculated by CMARC altogether.

4. METHOD OF ANALYSIS

In this report the chosen method of analysis was CFD (Computational Fluid Dynamics), and a program called CMARC, which will be described later in this chapter.
Experimental data for the UAV is available, obtained from scaled wind tunnel tests at ARTI's 3m diameter wind tunnel. This data will be compared with a fundamental analysis of the same model using the aforementioned CFD program. The further analyses can then be gauged against this data and comparisons between the configurations made.

Initially, the model is created in a program called LOFTSMAN, which is used for making geometries then meshing this geometry ready for analysis in CMARC. The results can then be examined in POSTMARC.
A brief description of the three programs is given below.

4.1 LOFTSMAN[1]

LOFTSMAN is a program for developing shapes for streamlined bodies, such as aircraft fuselages, canopies, nacelles and fairings; boat hulls; and lifting and control surfaces and keels, which will be referred to collectively as "wings". Its function is to define geometries and to export points, lines and wireframes in various formats.

LOFTSMAN is not a drawing processor or CAD program. It should be used before a CAD program, to create shapes in the first place. It is generally not practical or desirable to create shapes with a CAD program and then try to import them into LOFTSMAN in order, for instance, to generate meshes. Nevertheless, existing shapes can usually be recreated in LOFTSMAN with reasonable fidelity.

LOFTSMAN uses different methods for lofting bodies and wings, and generally does not process both simultaneously. Images of bodies and wings can be combined on the screen, but most operations are performed on bodies or the wings separately.

LOFTSMAN is supplied in two versions, a standard version and an enhanced version called LOFTSMAN/P. LOFTSMAN/P provides additional facilities for automatically generating formatted surface patches for input to Pmarc-12, CMARC and VSAERO.

Users unfamiliar with classical lofting techniques may at first find some aspects of body lofting and curved wing lofting confusing, particularly if they rely on the industry-standard procedure of using the program first to accomplish some urgent project, and consulting the documentation later. Defining arbitrary three-dimensional shapes is bound to be complicated, and LOFTSMAN does not entirely take over the job of designing things; it just greatly facilitates it.

4.2 CMARC[2]

The basic analytical functions of *Digital Wind Tunnel* (DWT) are identical to those of the DOS version of CMARC. An initial dialogue takes the place of CMARC's command line, and DWT provides an editor for inspecting and modifying the input file. DWT is slightly faster than DOS CMARC in full analyses, and much faster in large geometry-only analyses because of superior memory management.

faster than DOS CMARC in full analyses, and much faster in large geometry-only analyses because of superior memory management.

Beyond the services provided by DOS CMARC, DWT also provides 2D analysis of airfoils and a simulation-based approach to predicting static and dynamic longitudinal and lateral-directional stability.
CMARC and DWT use the same input file for geometry definition and run management, and provide similar options for overriding some run-control items.

4.2.1 PANEL METHOD

The three-dimensional model to be analysed consists of a closed surface immersed in a field of infinite extent. The surface itself, which is subdivided into a large number of generally rectangular panels, separates the field into inner and outer regions. Depending on the formulation of interest, either may be the subject of the analysis, the other remaining a fictitious flow. Most aerodynamic and hydrodynamic problems target the outer region. Flow is assumed to be incompressible, irrotational, and inviscid.

Velocity potentials in both regions are assumed to satisfy Laplace's equation:

$$\nabla^2\Phi = 0 \qquad \nabla^2\Phi_i = 0 \tag{1}$$

Applying Green's Theorem to both regions produces the following equation:

$$\Phi_P = \frac{1}{4\pi}\iint_{S+W+S_\infty}(\Phi-\Phi_i)\,\overline{n}\cdot\nabla\left(\frac{1}{\overline{r}}\right)\,dS \;-\; \frac{1}{4\pi}\iint_{S+W+S_\infty}\left(\frac{1}{\overline{r}}\right)\,\overline{n}\cdot(\nabla\Phi-\nabla\Phi_i)\,dS \tag{2}$$

The first integral represents the disturbance potential from a surface distribution of doublets whose strength is $(\Phi-\Phi_i)$ per unit area. The second integral represents the contribution from a surface distribution of sources whose strength is $-\overline{n}\cdot(\nabla\Phi-\nabla\Phi_i$ per unit area.

Since the perturbation potential at infinity becomes essentially zero, only the potential due to the uniform onset flow remains; the source term for the wake also disappears, allowing simplification of (2) as follows:

$$\Phi_P = \frac{1}{4\pi}\iint_{S}(\Phi-\Phi_i)\,\overline{n}\cdot\nabla\left(\frac{1}{\overline{r}}\right)\,dS \;-\; \frac{1}{4\pi}\iint_{S}\left(\frac{1}{\overline{r}}\right)\,\overline{n}\cdot(\nabla\Phi-\nabla\Phi_i)\,dS + \frac{1}{4\pi}\iint_{W}(\Phi_U-\Phi_L)\,\overline{n}\cdot\nabla\left(\frac{1}{\overline{r}}\right)\,dS + \phi_{\infty P} \tag{3}$$

Integrals become singular at point P if it lies on the surface. The point is excluded from the integration by assuming a hemispherical deformation of the surface with P as its centre. Evaluating the integral for this deformation and allowing its radius to shrink to zero, the contribution at P becomes $1/2(\Phi-\Phi_i)_P$ if P is an exterior point and the negative of that value otherwise.

Thus for interior surface points (3) becomes:

$$\Phi_P = \frac{1}{4\pi}\iint_{S-P}(\Phi-\Phi_i)\,\overline{n}\cdot\nabla\left(\frac{1}{\overline{r}}\right)\,dS \;-\; \frac{1}{4\pi}\iint_{S}\left(\frac{1}{\overline{r}}\right)\,\overline{n}\cdot(\nabla\Phi-\nabla\Phi_i)\,dS \qquad (4)$$
$$+\;\frac{1}{4\pi}\iint_{W}(\Phi_U-\Phi_L)\,\overline{n}\cdot\nabla\left(\frac{1}{\overline{r}}\right)\,dS \;+\; \phi_{\infty_P} \;-\; \frac{1}{2}(\Phi-\Phi_i)_P$$

An internal Dirichlet boundary condition is used to solve (4). The total potential Φ can be regarded as the sum of the onset potential ϕ_∞ and a perturbation potential $\phi = \Phi - \phi_\infty$. The onset potential is used for the fictitious flow, because surface singularities then tend to be smaller than if the potential in the fictitious flow is zero (since the singularities provide only the perturbation potential rather than the total potential).

For points P inside the surface, (4) can be rewritten as:

$$0 = \frac{1}{4\pi}\iint_{S-P}\phi\;\overline{n}\cdot\nabla\left(\frac{1}{\overline{r}}\right)\,dS \;-\; \frac{1}{4\pi}\iint_{S}\left(\frac{1}{\overline{r}}\right)\,\overline{n}\cdot(\nabla\Phi-\nabla\phi_\infty)\,dS \qquad (5)$$
$$+\;\frac{1}{4\pi}\iint_{W}(\Phi_U-\Phi_L)\,\overline{n}\cdot\nabla\left(\frac{1}{\overline{r}}\right)\,dS \;-\; \frac{1}{2}\,\phi_P$$

Referring to (2), we can write for doublet and source strengths:

$$4\,\pi\,\mu \;=\; \phi \;=\; (\Phi-\phi_\infty \qquad (6)$$

$$4\,\pi\,\sigma \;=\; -\,\overline{n}\cdot(\nabla\Phi-\nabla\phi_\infty \qquad (7)$$

Given (7), if the normal velocity at the surface is zero or has some known value we can write for surface source strengths:

$$\sigma \;=\; \frac{1}{4\pi}\;(V_{norm}-\overline{n}\cdot\overline{V}_\infty \qquad (8)$$

The surface normal velocity is either zero or is defined by the user; and the onset velocity vector is known. Combining (6) and (7) with (5) yields the following integral equation in which the doublet strength over the surface is unknown:

$$0 = \left[\iint_{S-P}\mu\;\overline{n}\cdot\nabla\left(\frac{1}{\overline{r}}\right)\,dS - 2\pi\mu_P\right] \;+\; \iint_{S}\left(\frac{\sigma}{\overline{r}}\right)\,dS \;+\; \iint_{W}\mu_W\;\overline{n}\cdot\nabla\left(\frac{1}{\overline{r}}\right)\,dS \qquad (9)$$

The potential at any point P can be expressed as:

$$\Phi_P = \left[\iint_{S-P}\mu\;\overline{n}\cdot\nabla\left(\frac{1}{\overline{r}}\right)\,dS + \;K\,\mu_P\right] + \iint_{S}\left(\frac{\sigma}{\overline{r}}\right)\,dS \;+\; \iint_{W}\mu_W\;\overline{n}\cdot\nabla\left(\frac{1}{\overline{r}}\right)\,dS \;+\; \phi_{\infty_P} \qquad (10)$$

K may have one of three values. If P is not on the surface, K is zero. If P lies on a smooth part of the outer or inner surface, K becomes 2π or -2π respectively. If P lies on a crease in the surface forming a solid angle, K is equal to the angle.

When the surface is broken up into panels, (9) may be written in discretised form, creating surface integrals over each panel. Being a low order panel method, CMARC assumes that the strengths of sources and doublets are constant over a panel. Doublet and source strengths can therefore be factored out of the discretised integrals.

Surface integrals are summed for all panels, P having been set at the centred of one panel on the inner surface. The surface integral for the panel containing P is zero, leaving only the $-2\pi\mu_P$ term in the bracketed part of (9). For all other panels, the surface integral may be used and the $-2\pi\mu_P$ term is zero because P is not on the panel. This process is repeated for each panel, producing a set of simultaneous linear equations to be solved for the unknown doublet strength on each panel. The surface integrals represent the velocity potential influence coefficients CJK and BJK per unit singularity strength for each panel K acting on the control point of a given panel J. Thus (9) becomes:

$$\sum_{K=1}^{N_S}(\mu_K\, C_{JK}) + \sum_{K=1}^{N_S}(\sigma_K\, B_{JK}) + \sum_{L=1}^{N_W}(\mu_{W_L}\, C_{JL}) = 0\Big|_{J=1,\ N_S} \tag{11}$$

where

$$B_{JK} = \iint_K \frac{1}{\bar{r}}\ dS \tag{12}$$

and

$$C_{JK} = \iint_K \bar{n}\cdot\nabla\left(\frac{1}{\bar{r}}\right)\ dS \tag{13}$$

$$C_{JJ} = -2\pi$$

Equations (12) and (13) can be solved for all panels to form the coefficient matrix, since they are functions of model geometry only. (See reference 6 for solution to these equations.) Source values, which are known, can be transferred to the right side of the matrix equation. Wake doublet values can be found as functions of surface doublet values, leaving the surface doublet strengths the only unknowns.

Equation (11) is solved by first determining the velocity potential influence coefficient matrix elements CJK for the unknown doublet strengths and BJK for the known source strengths. For nearby panels, an exact solution is obtained by assuming that the singularities are distributed over the panel, and integrating over the panel surface. Distant panels are treated as though the entire panel were a point source or doublet. A characteristic panel dimension, approximately the average of its width and height, is multiplied by the far-field factor to obtain the crossover distance between nearby and distant panels. The default value is 5.0; a lower value increases speed at the expense of accuracy, a higher one vice versa.

Having obtained the influence coefficients, CMARC solves iteratively for the unknown doublet strengths. Convergence is directed by applying to the current solution vector a correction vector derived from the history of previous solutions. An iteration limit and a tolerance, both of which are set by the user in the input file, control termination of the convergence. The tolerance is the percentage difference between successive values of the element in the solution vector that shows the largest change between successive iterations. Values between 0.01 and 0.0005 have proven satisfactory; 0.0005 is the default. Convergence usually occurs in between 50 and 150 iterations on the first time step, and in fewer iterations thereafter.

When the unknown doublet strengths have been obtained, the singularities on all panels are known, and it is possible to evaluate the velocities at the control points of the panels. Normal velocities are either zero or some value specified by the user. Surface tangential velocities in the local co-ordinate system are obtained by differentiating the doublet strengths in the appropriate direction for each tangential component of velocity. A resultant velocity is obtained by transforming these results into the global co-ordinate system, and a pressure coefficient is derived from it using the following equation:

$$C_{P_K} = 1 - \frac{V_K^2}{V_\infty^2} + \left(\frac{2*4\pi}{V_\infty^2}\right)\left(\frac{\mu(t)-\mu(t-1)}{\Delta t}\right) \qquad (14)$$

The last term in (14) represents the unsteady term, $d\Phi/dt$.

4.2.2 COMPUTATION OF INDUCED DRAG

CMARC computes induced drag in two ways. One is by integrating surface pressures. It must be noted that because of the rapid pressure gradient at the leading edges of lifting surfaces, a large number of chordwise panels is needed to resolve induced drag accurately.

The second method is the so-called Trefftz plane analysis, which involves evaluating the following integral along a line of intersection between the wake and a plane normal to the velocity vector and located far (e.g. 15-20 chord lengths) downstream of the lifting surface:

$$D_i = \frac{\rho}{2}\int_{wake} \Gamma V_n dl \qquad (15)$$

V_n is the normal component of the induced velocity on the wake at the Trefftz plane, and Γ is the circulation on the lifting surface at the corresponding spanwise location.

An accurate solution for induced drag from the Trefftz plane analysis requires that the wake at the Trefftz plane be drag-free. Either a rolled-up wake or a simple flat sheet aligned with the free stream fulfils this requirement, but it may be necessary to use the rolled-up (i.e. flexible) wake option when a model involves several non-planar lifting surfaces.

4.3 POSTMARC[3]

Postmarc is merely the postprocessing part of this set up, it simply allows the various output files from CMARC to be viewed and also some limited calculations to be done.
Here it is possible to view contour plots of pressure coefficient, both solid and line, wakes and also streamlines too.

5. THE MODEL

The basic UAV model was produced using LOFTSMAN in conjunction with technical drawings of the vehicle. The way this program operates it is necessary to firstly produce ASCII files that can be read into LOFTSMAN and from here on in edited and altered if necessary.
It is the case that two types of file exist, body data files (.LFT) and wing data files (.WI). As you can imagine body data files are usually objects such as fuselages, whilst anything containing an aerofoil section can be classed as a wing data file.

Body files are often the most complex shape so can be viewed in LOFTSMAN by segmenting along a the length of the body and producing cross sections such as in Fig. 1. This can be viewed in three-dimensions and gives a feel of how the body looks. In this example it is the fuselage of the Sojka. If something does not look correct it can be easily altered.

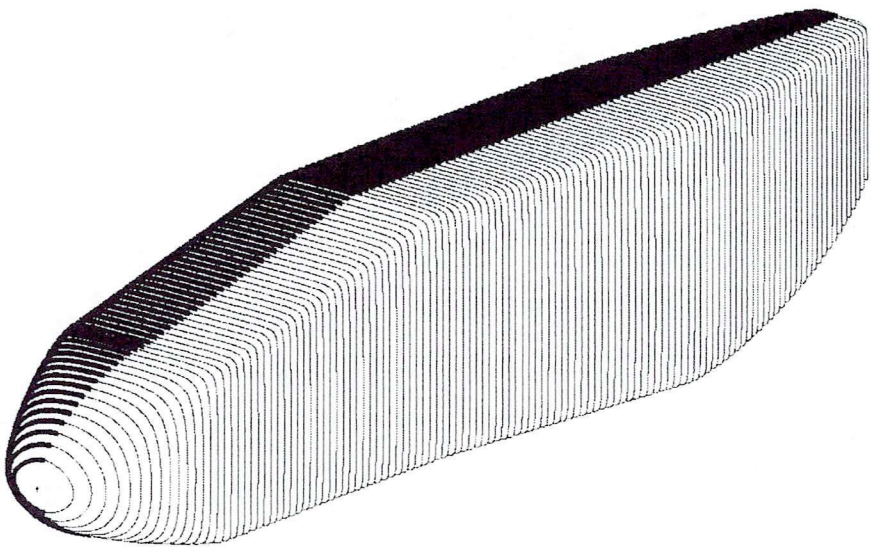

Fig. 1 - UAV fuselage

Once completely satisfied with the files that have been assembled together to form the basic skeleton or geometry of the model, as in Fig. 2, it is then necessary to move to the next stage and mesh the surface of the body. LOFTSMAN mainly deals with symmetric bodies, so it has the capability to simply mesh half a body and this is what occurs in this case. In this situation it is only the starboard side of the model that is dealt with.
The original Sojka was formed using a combination of 5 data files, 2 body data files and 3 wing data files, as follows:

1. Fuselage
2. Main Wing
3. Tailboom
4. Tailfin
5. Horizontal Stabiliser

It should be pointed out at this stage, that the UAV is powered by a centrally located pusher propeller. This was not modelled because CMARC simply cannot analyse a propeller, though LOFTSMAN did have a facility for meshing such an appliance. If Digital Wind Tunnel was

used in place of CMARC then a fuller analysis could have been undertaken with the propeller present. Although for comparison purposes a propeller was also absent from the wind tunnel tests.

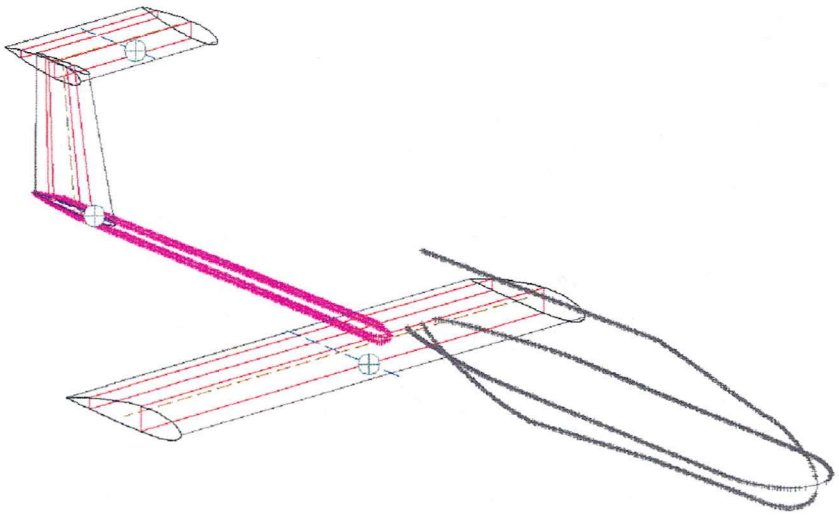

Fig. 2 - UAV geometry

Meshing with LOFTSMAN is a fairly simple procedure, though at times can become complex if the facilities available are stretched and manual meshing is required. The model had to be manipulated slightly, especially at points of intersection, as there are certain circumstances under which meshing of intersecting parts becomes messy with lots of odd shaped elements. Once complete, the mesh should resemble something like that of Fig. 3.

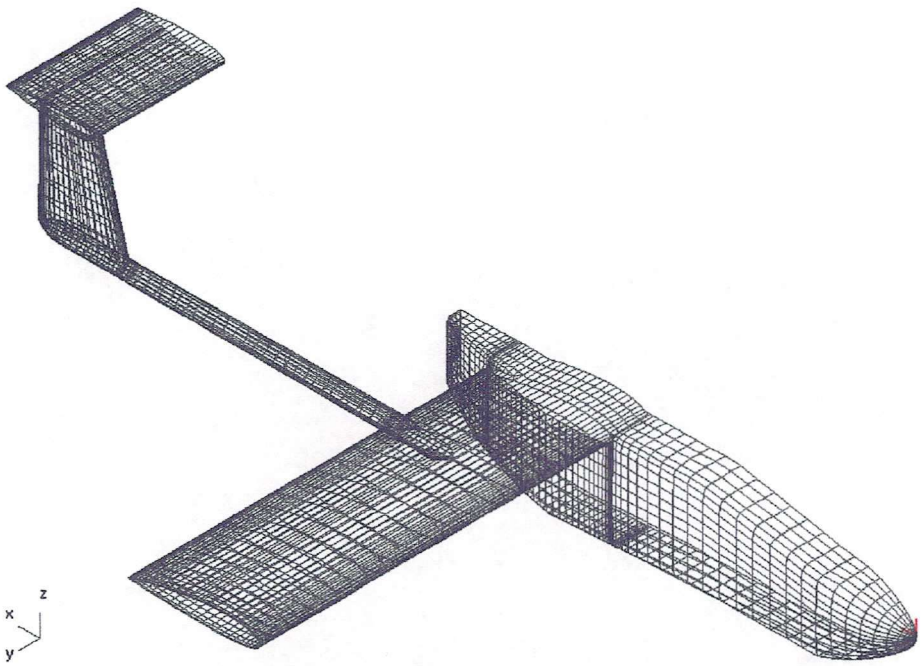

Fig. 3 - Meshed geometry

Once the half model has been meshed it can then be run to test the geometry which also allows the whole body to be viewed and inspected, as in fig. 4.

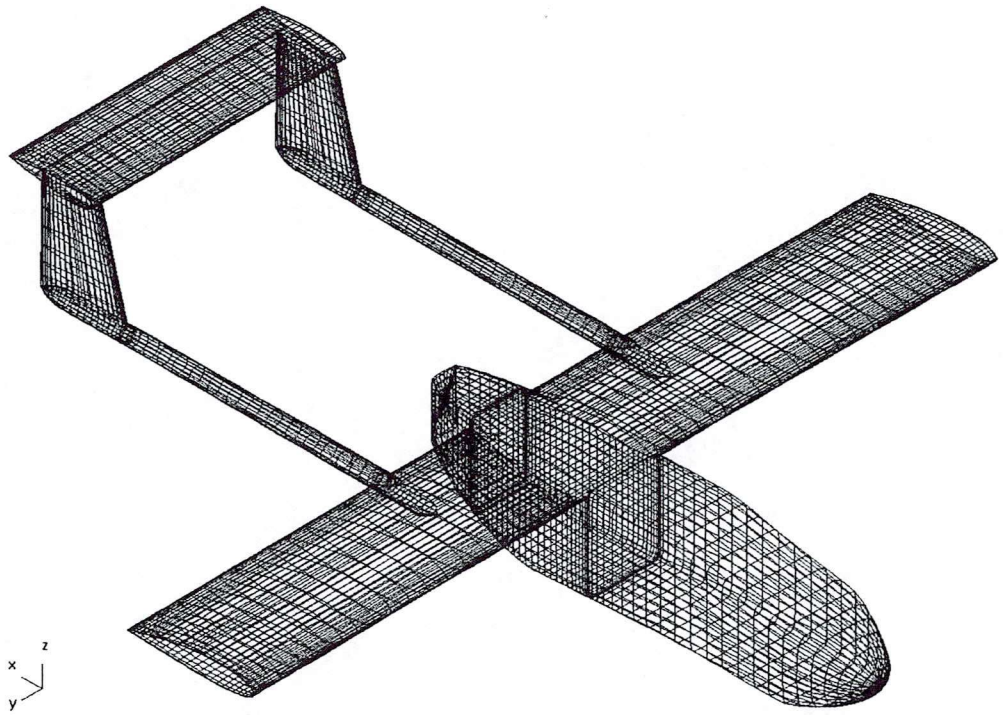

Fig. 4 - UAV configuration with tailbooms

The next stage involves meshing of the wake. It is necessary to implement a wake in order for the surface to generate lift. Flow must be prevented from circulating around the trailing edge. CMARC uses an imaginary membrane called a "wake" to separate upper-surface from lower-surface flow. The wake may be thought of as the "downwash sheet." If no wake is provided for a lifting surface, the pressure distributions on it and on the rest of the model will be incorrect.

CMARC provides several options for dealing with the wake. It may be fully pre-defined, or it may be generated by CMARC from a separation line specified by the user. It may be rigid or flexible. Finally, the number of time steps in wake development, and their duration, may be defined
For a simple wing model, at least, differences in results between various wake options are very slight; rounded to 2 decimal places, they all but disappear.

In LOFTSMAN the simplest wake case is that of a wing analysed in isolation. The wake is normally modelled as a flat surface emanating from the trailing edge. This is concisely done by identifying the wing trailing edge as the line of attachment of the wake and using this to create a copy of the attachment line some distance downstream. CMARC fills in the intermediate sections. A wake should extend about 20 chord lengths behind the lifting surface.

To define a wake attachment line, you must identify either the edge of a patch or the panel edge line within the patch along which the wake will be attached.
Multiple wakes may intersect each other, but a wake must not intersect a body except along a defined separation line.

If the model includes a horizontal tail, it may be necessary to adjust the fuselage panelling to provide a wing wake attachment line that does not intersect the horizontal tail. Note that the portion of the wing wake emanating from the wing trailing edge may be horizontal or may be adjusted upward and downward, within reasonable limits, as desired. If LOFTSMANs wake-generating procedure is used with a specified wake downwash angle, the portion of the wake between the wing root and the plane of symmetry will be curved upward or downward as necessary to connect the bulk of the wake surface with the fuselage attachment line.

It is not necessary to provide vertical surfaces with wakes unless a case is run in a yawed condition or the vertical surfaces produces lift in unyawed flight, like a winglet.

The line (Wake Separation Line) along which the wake separates from the body is defined by one or more lines of code in the input file. The line may begin at the plane of symmetry or at a wingtip, but it must progress continuously in the same direction throughout its definition. The wake should extend all the way to the plane of symmetry; otherwise a second set of tip vortices will form on the inboard edges of the wake.

Once the wake has been defined the model can then be run fully in CMARC and the results analysed in Postmarc.

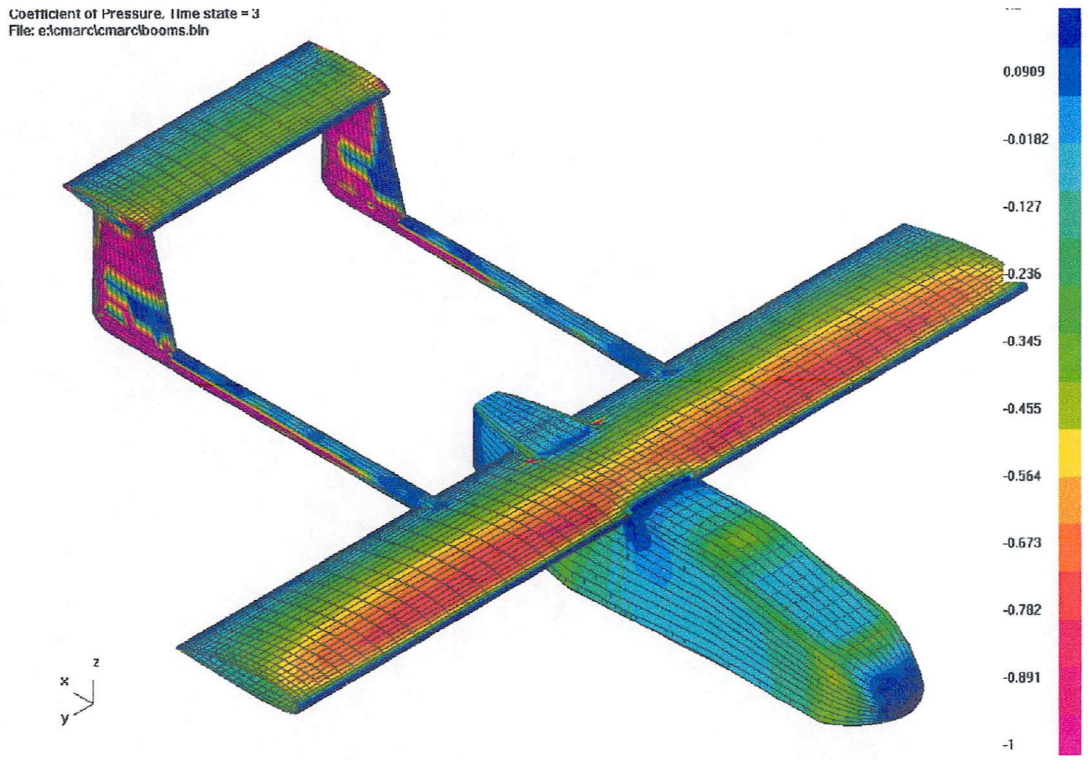

Fig. 5 – Pressure coefficient plot of UAV with tailbooms

Fig. 5 shows the pressure coefficient plot obtained from the first run for the UAV model. Analysis of the plot highlights several unwanted abnormalities around the aft region of the model. Some highly negative pressure coefficients, even more negative than the suction region of the main wing, are apparent on the vertical fins of the tail. These should simply not be here for various reasons. Primarily as the tail is for stability and not lift generation and secondly because the profile is a NACA 0012, which should not have such negative values in the first due to the lack of extreme curvature.

The tailboom has a mixture of excessively high and low values and is very irregular in its distribution.

The reason for these abnormalities becomes apparent on perusal of fig. 6. The wake is severely distorted and the streamlines appear to be forming highly irregular flow patterns. This then seems to revert back to the model, which in turn is causing these irregular pressure coefficients. The presence of the tailbooms complicate matters a great deal, in reality these booms are slightly tapered, though for the purposes of CMARC they were tapered rather more sharply. This is simply because CMARC produces wakes along panel edges, and in theory if the panels are parallel to the flow they effectively have zero area. The tapering should be sufficient to eradicate this problem, although for some reason in this case it was simply not possible and the tailboom s where completely removed from the model without any detrimental effect, in fact, quite the opposite. The pressure coefficient plots are more realistic, the wake problem disappears and the figures are similar to those of the experimental value. All configurations now with tailbooms were then chosen to be modelled without tailbooms and it was accepted the results were still sufficiently good for this to be acceptable. Altogether 5 configurations of UAV were examined. Firstly, the original UAV, this was used to validate CMARC and provide a benchmark of comparison for the other configurations. Secondly, was the exact same UAV except instead of the NACA 2415 main wing profile this one had MS 0313. The third configuration was identical to the second, except a longer span was present. The last two configurations were completely different to the previous three and could be termed as groundbreaking or futuristic. The fourth configuration utilised a single, lengthened fuselage removing the need for tailbooms altogether, and employing a V shaped tail. The fifth and final configuration employed a delta wing design and also the tail booms along with a V tail with the join situated at the top of the tail.

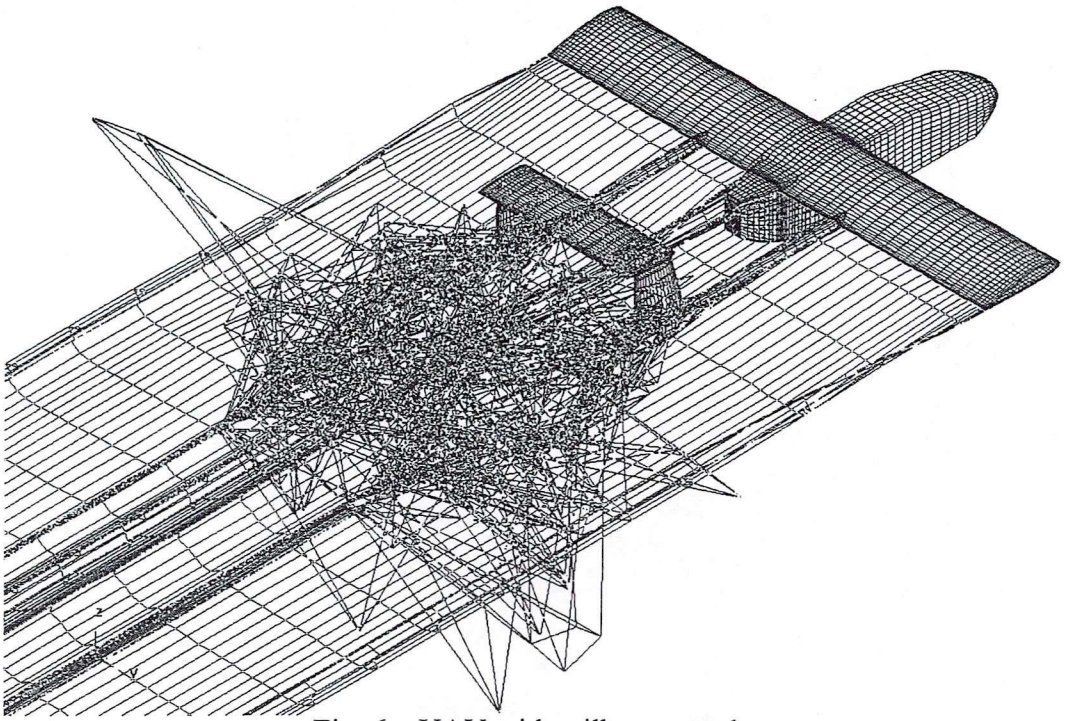

Fig. 6 – UAV with tailbooms wake

The following diagrams are simply the resultant meshes of the 5 models used in the analysis. For three-dimensional diagrams of the meshed models please refer to Appendix A.

5.1 UAV CONFIGURATION WITHOUT TAILBOOMS

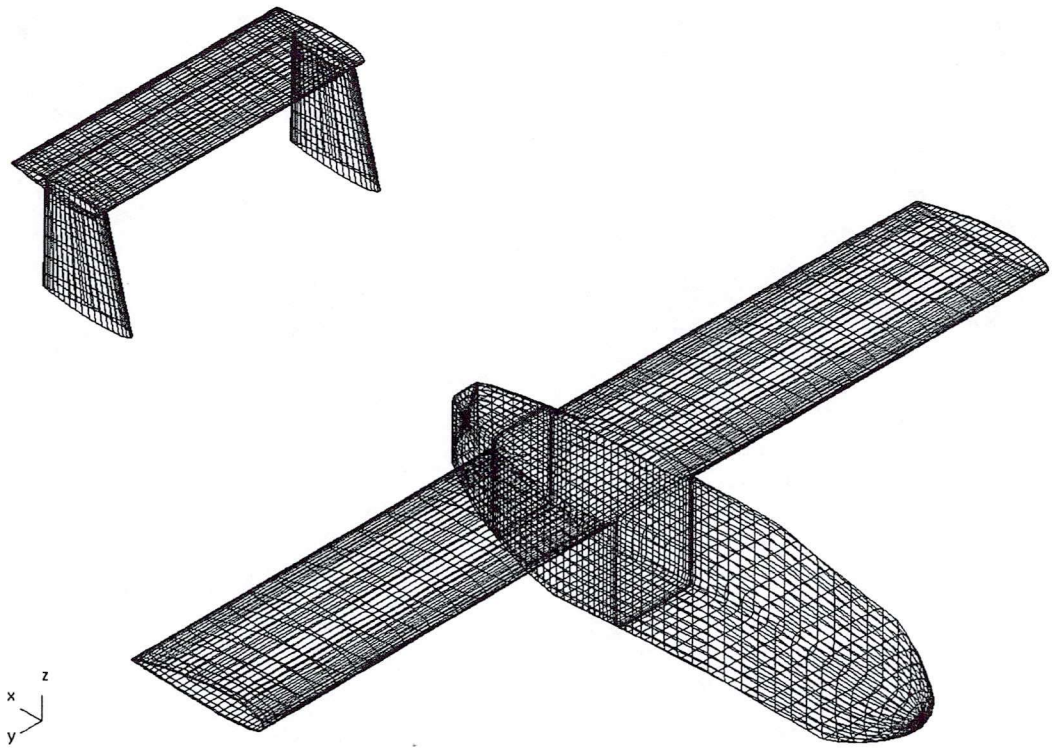

Fig. 7 – Perspective view of UAV configuration without tail booms

5.2 UAV CONFIGURATION WITH MS 0313 WING PROFILE

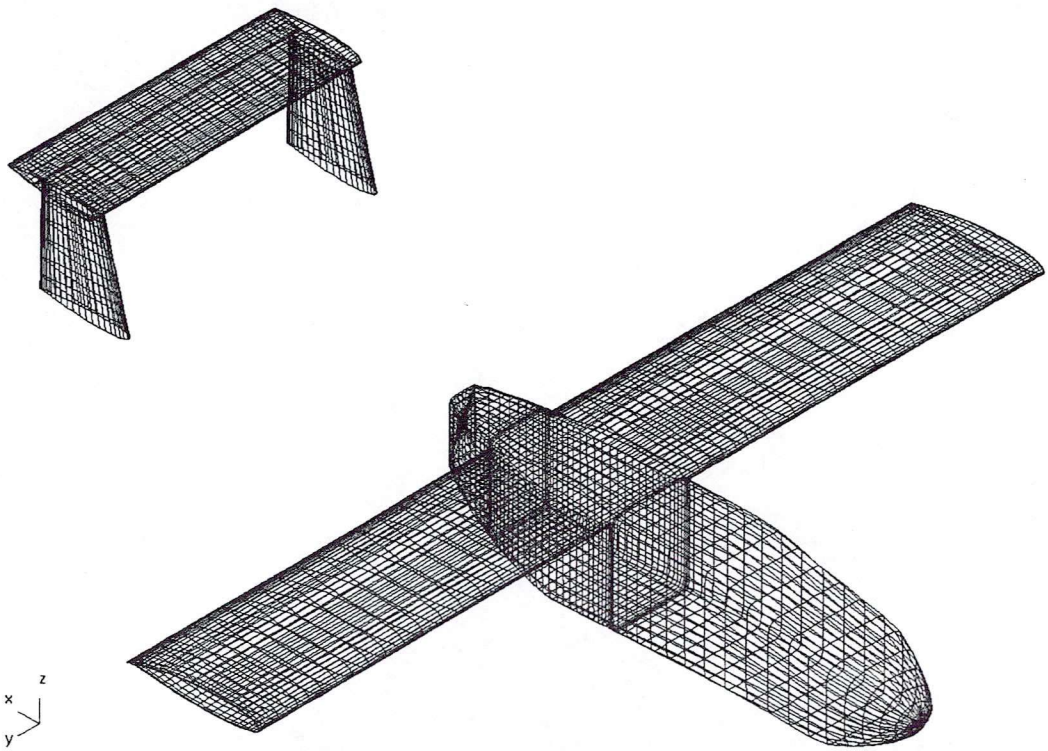

Fig. 8 – Perspective view of UAV MS 0313

5.3 UAV CONFIGURATION WITH MS 0313 PROFILE AND INCREASED SPAN

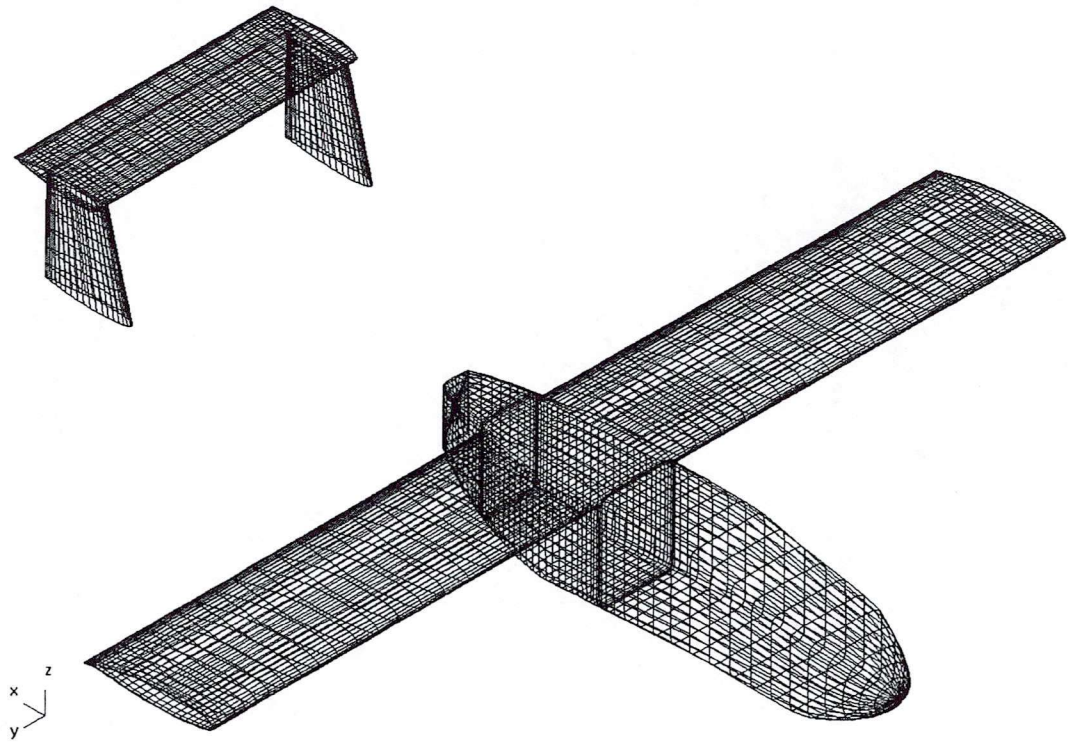

Fig. 9 – Perspective view of UAV MS 0313 with increased span

5.4 NEW UAV CONFIGURATION 1

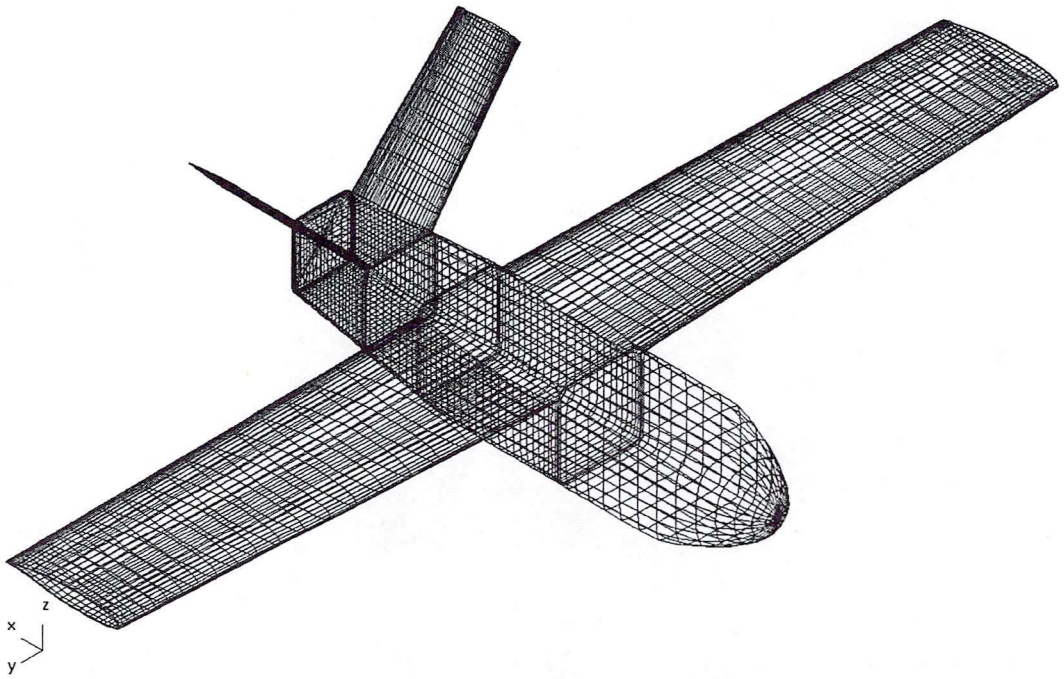

Fig. 10 – Perspective view of new UAV configuration 1

5.5 NEW UAV CONFIGURATION 2

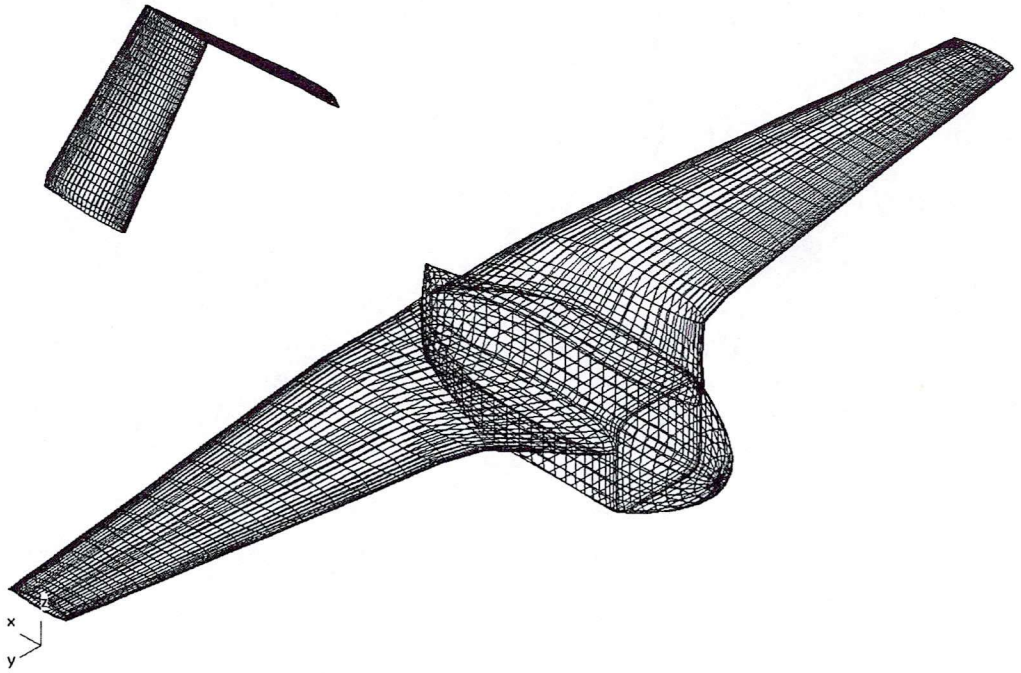

Fig. 11 – Perspective view of new UAV configuration 2

6. RESULTS

This section displays a summary of the results achieved from the CFD calculations run at ARTI.
The majority of this section comprises of the pressure coefficient plots of the analysis and the corresponding wakes. The calculations were carried out over the range of -5° up to stall or failure of the results. Rather than simply plot every result of every degree, it was chosen to simply do a summary of the results and display the results from -5° up to $+10^{\circ}$ showing the results at 5° intervals. This adequately allows any phenomena to be seen that may be occurring, the wakes are necessary for reasons that will become apparent.

Wind tunnel tests on the UAV were carried out, also at VZLU. These will serve as a comparison for the CFD data of the original UAV model and from this the subsequent models can then be compared with this original UAV CFD model. From this it can ascertained as to the performance and characteristics of the configuration with respect to the original and in turn whether or not any improvements can be attained by a changes in design.

Yaw is neglected throughout the entire analysis.

6.1 CONFIGURATIONS AT 0° ANGLE OF ATTACK

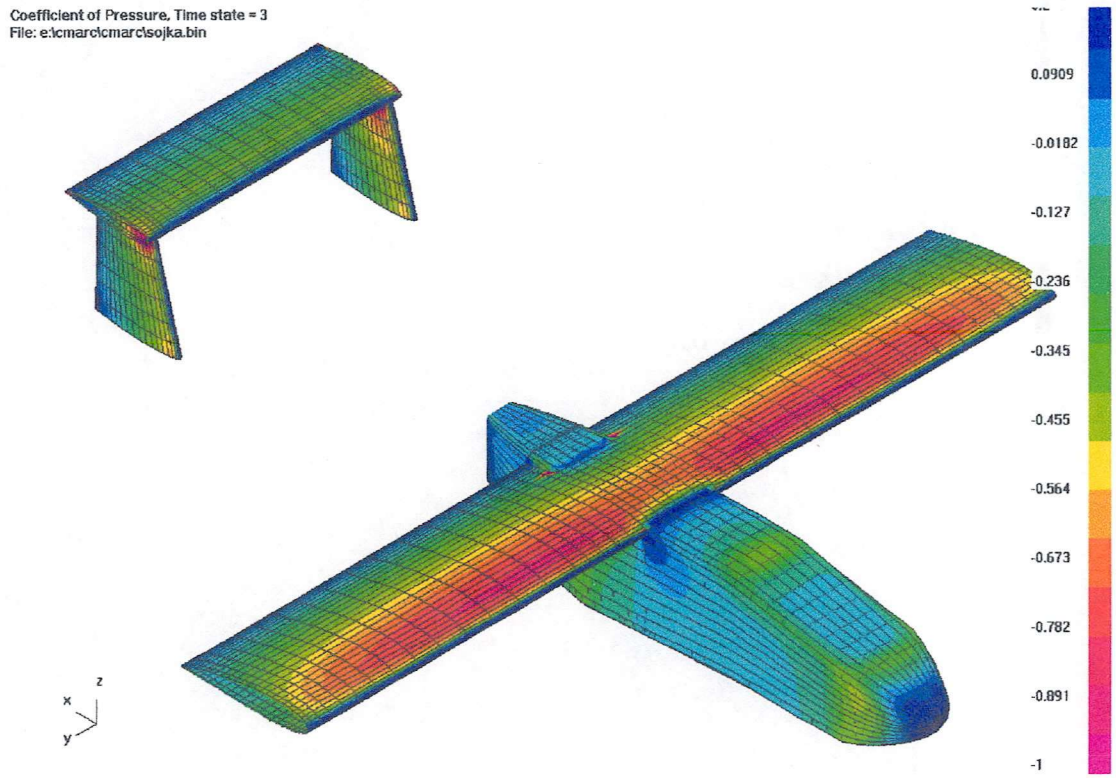

Fig. 12 – Original UAV pressure coefficients at 0° angle of attack

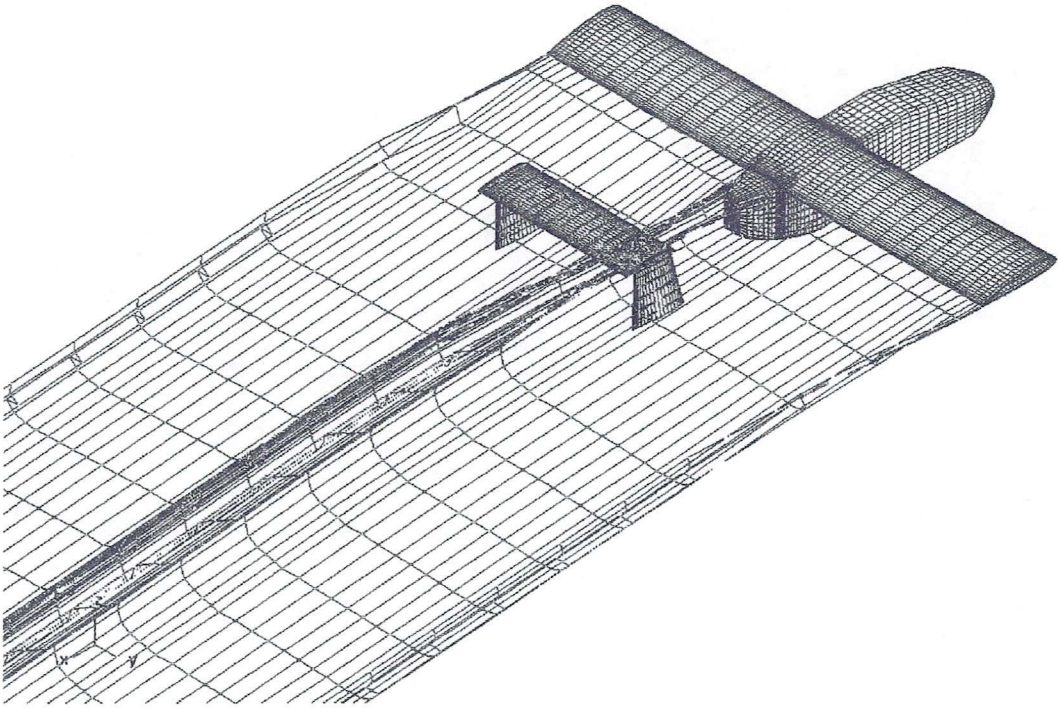

Fig. 13 – Original UAV wake 0° angle of attack

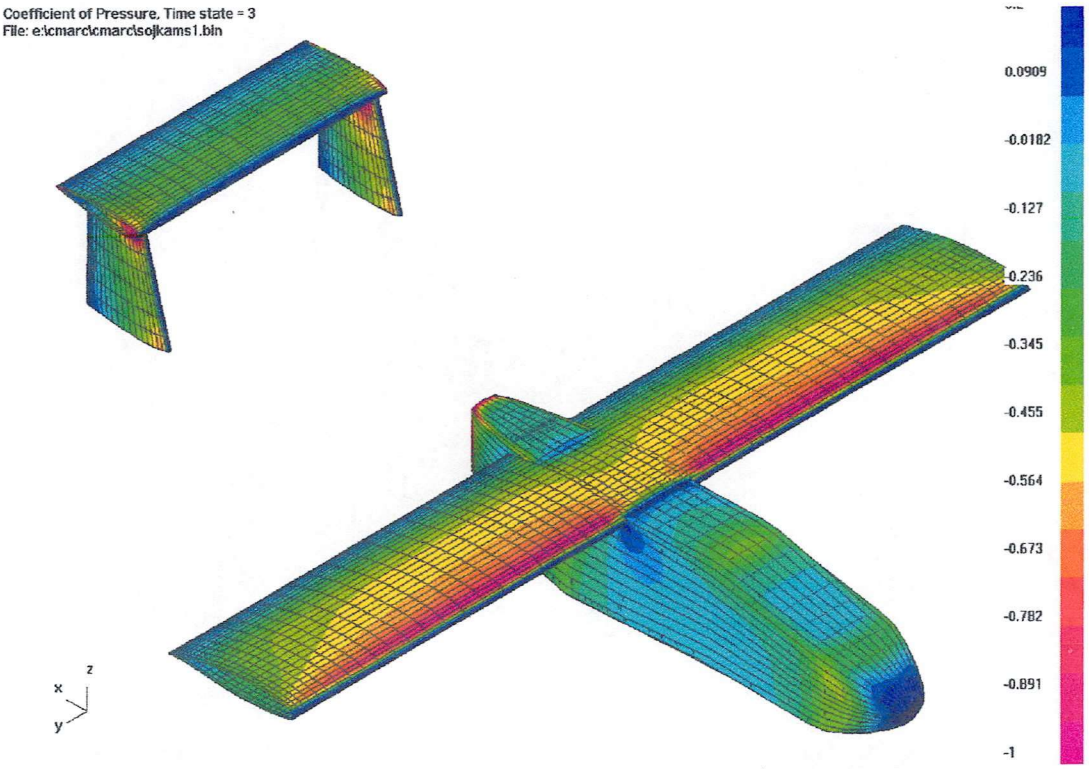

Fig. 14 - UAV MS 0313 pressure coefficients at 0° angle of attack

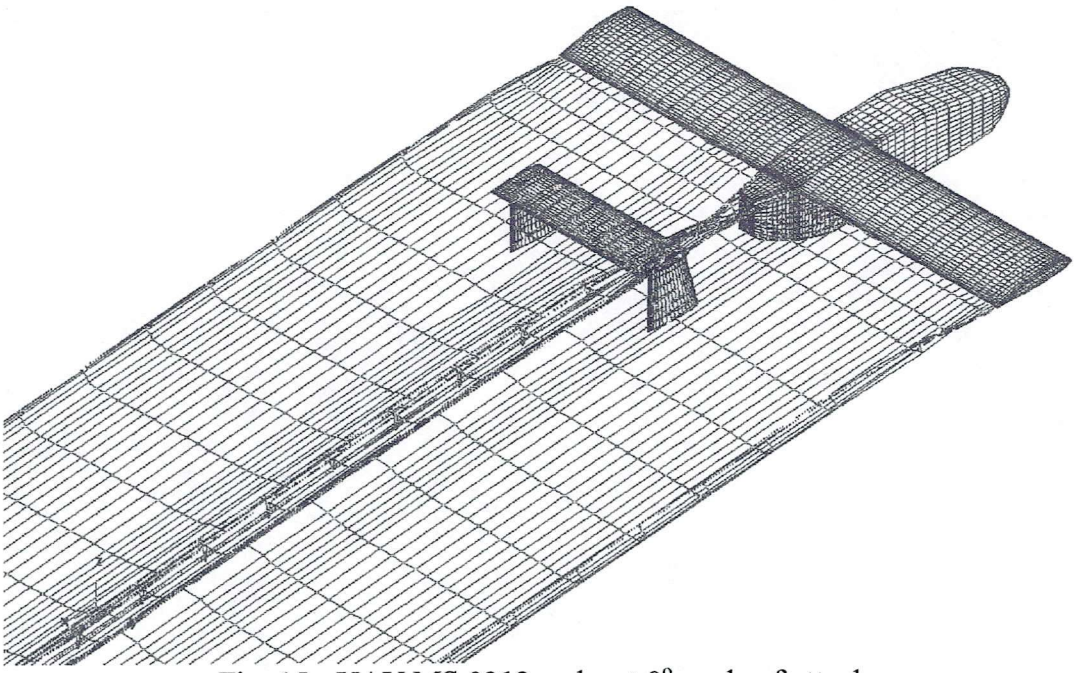

Fig. 15 - UAV MS 0313 wake at 0° angle of attack

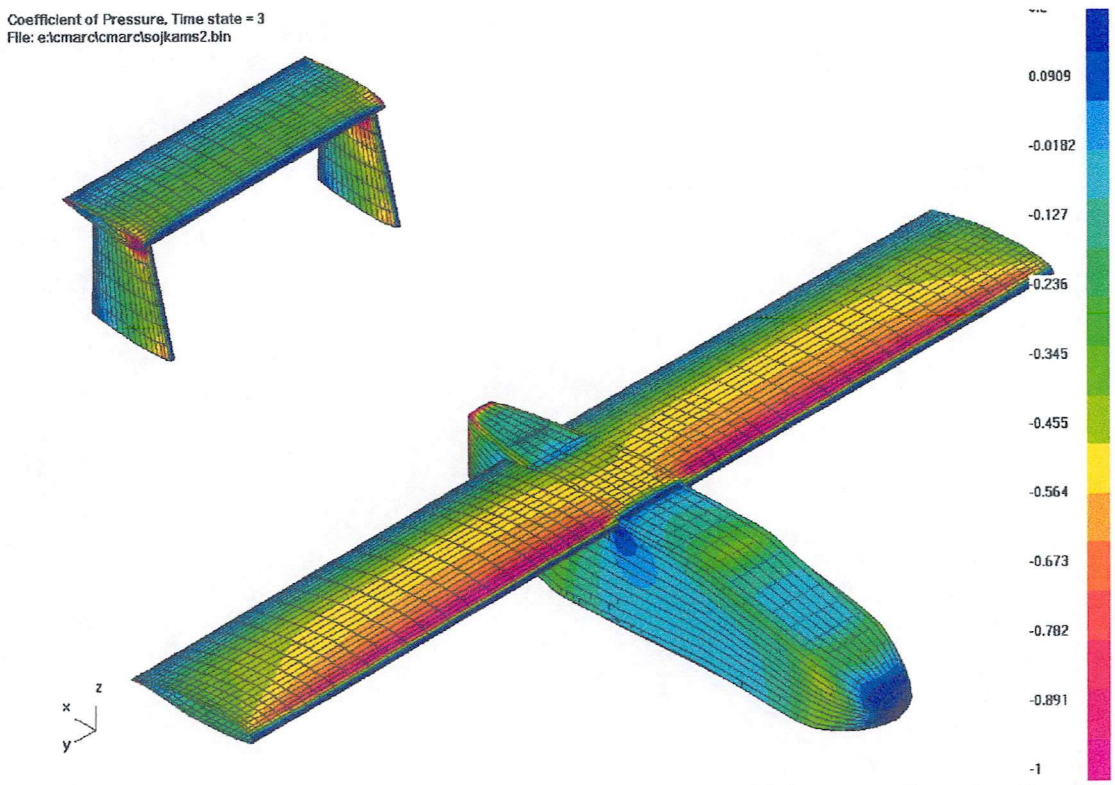

Fig. 16 - UAV MS 0313 with increased span pressure coefficients at 0° angle of attack

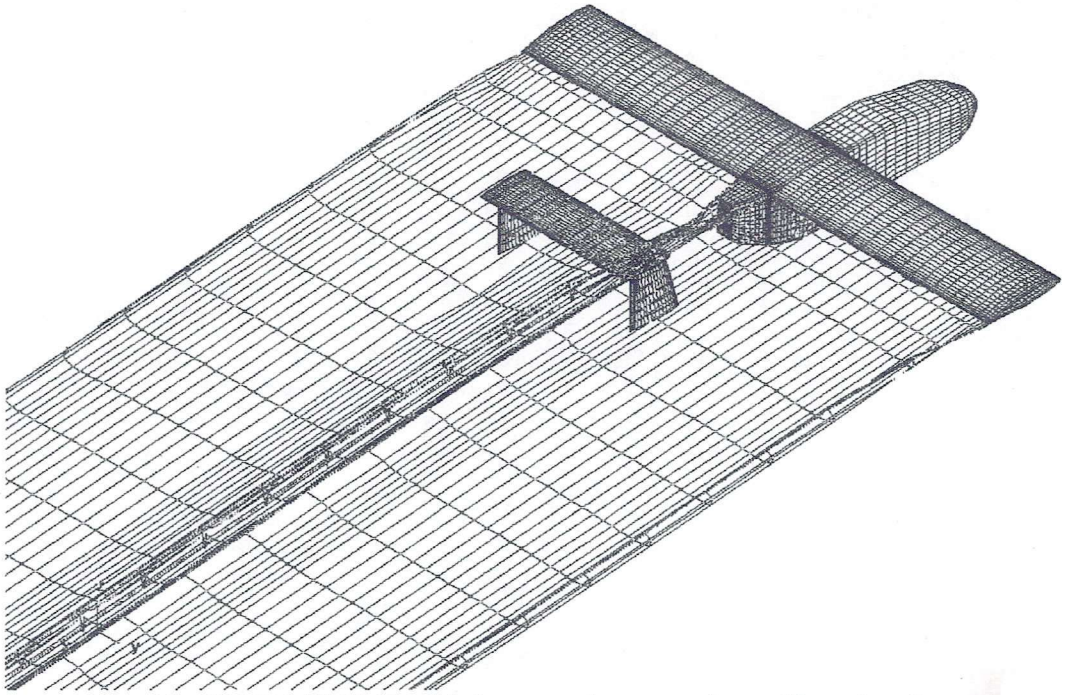

Fig. 17 - UAV MS 0313 with increased span wake at 0° angle of attack

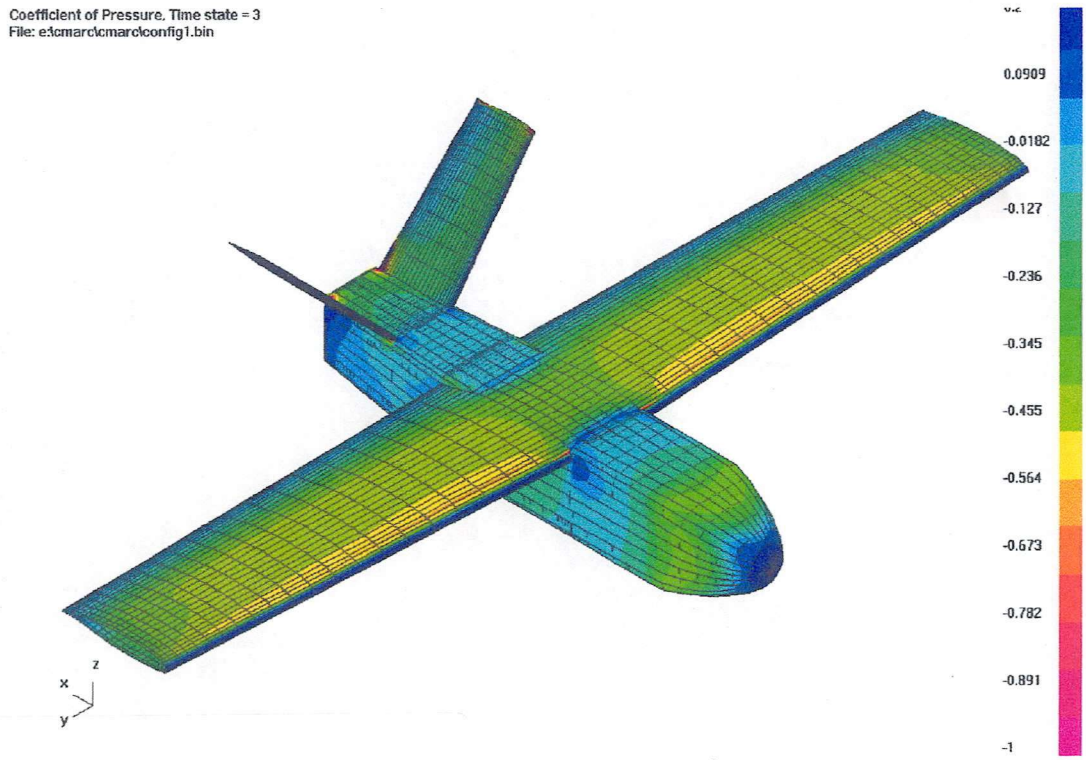

Fig. 18 - New UAV configuration (1) at 0° angle of attack

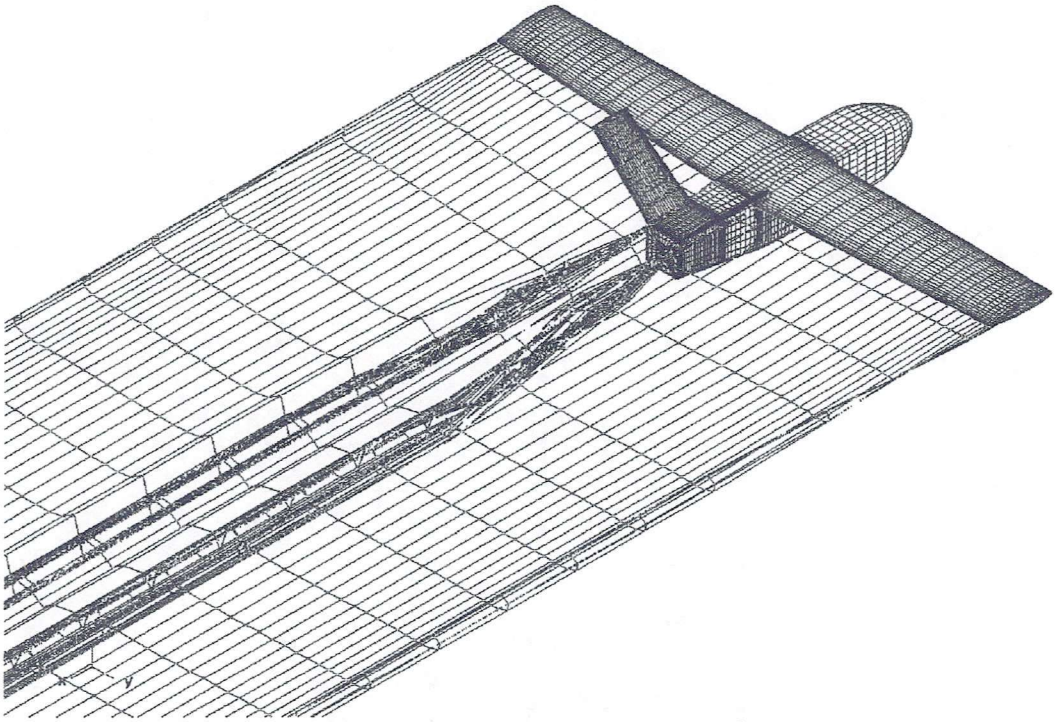

Fig. 19 - New UAV configuration (1) wake at 0° angle of attack

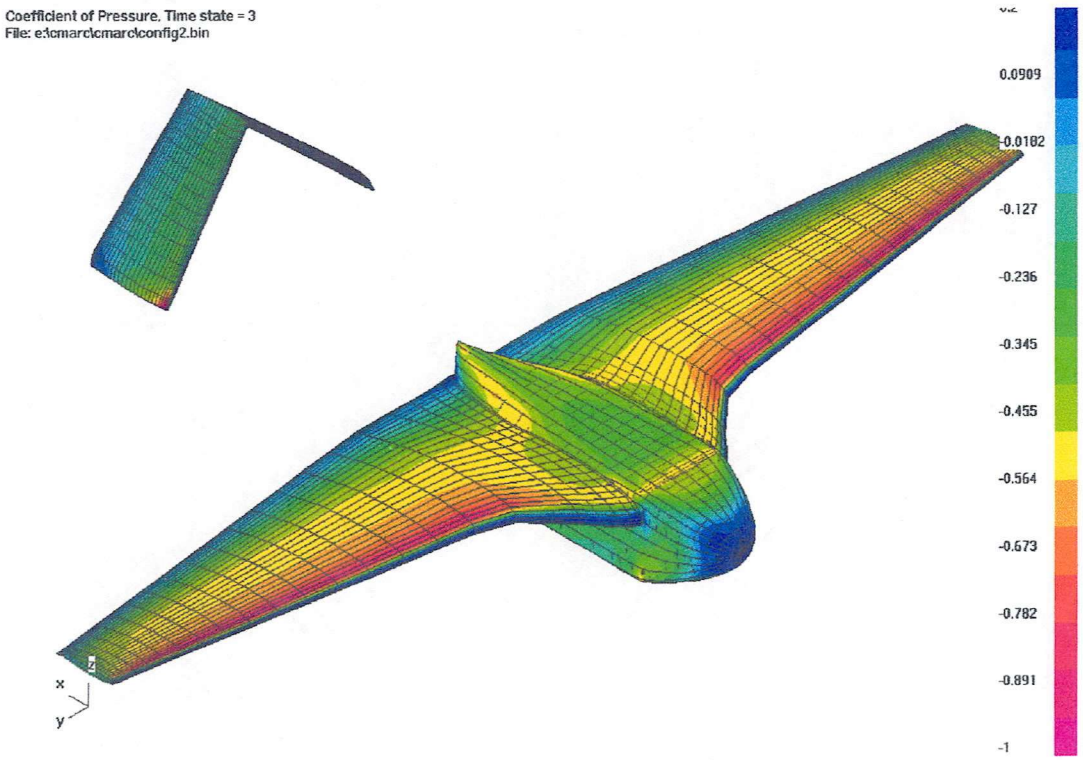

Fig. 20 - New UAV configuration (2) at 0° angle of attack

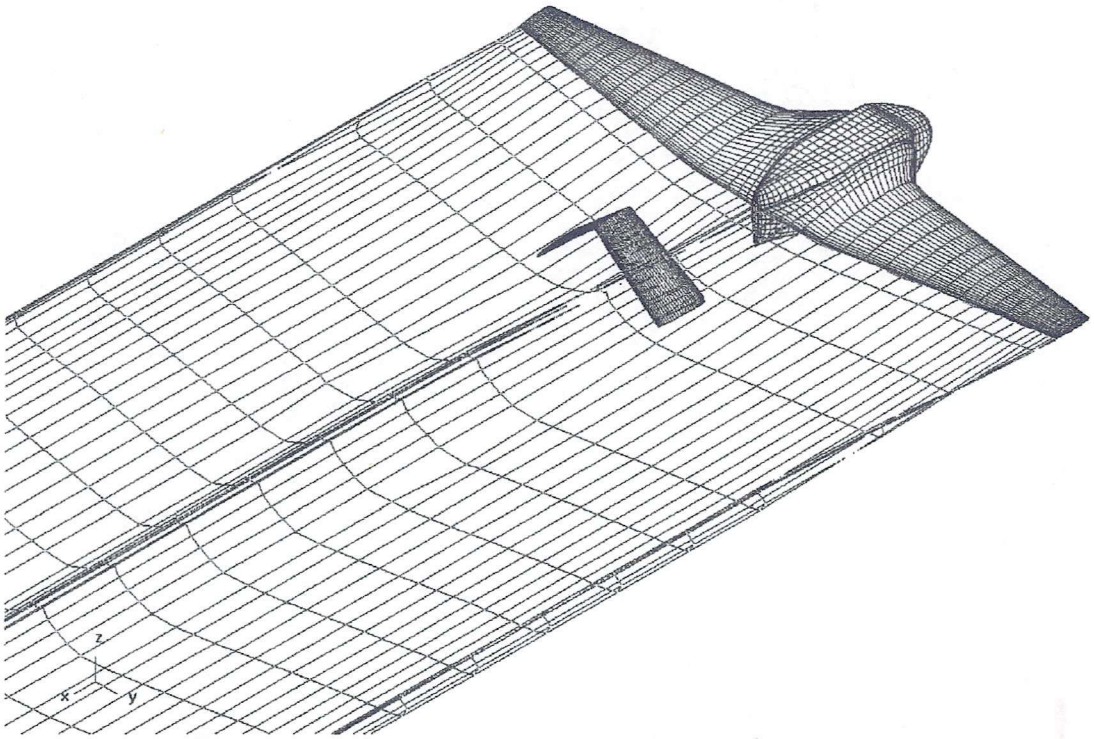

Fig. 21 - New UAV configuration (2) wake at 0° angle of attack

6.2 CONFIGURATIONS AT 5° ANGLE OF ATTACK

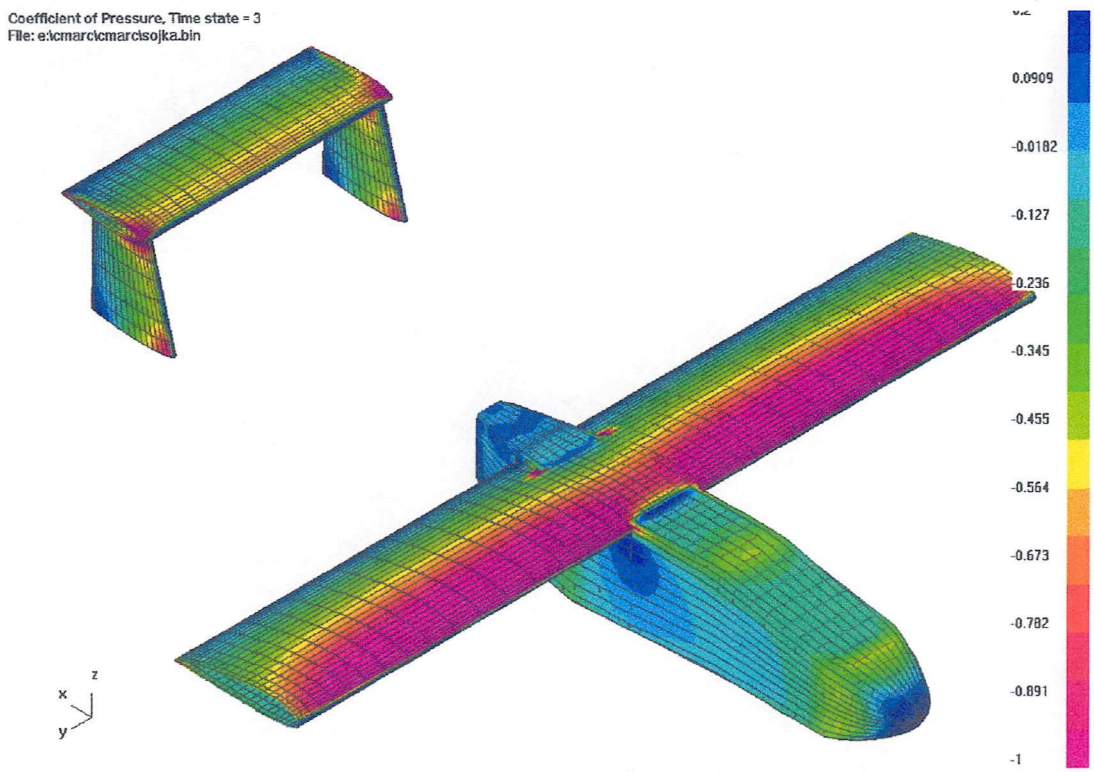

Fig. 22 – Original UAV at 5° angle of attack

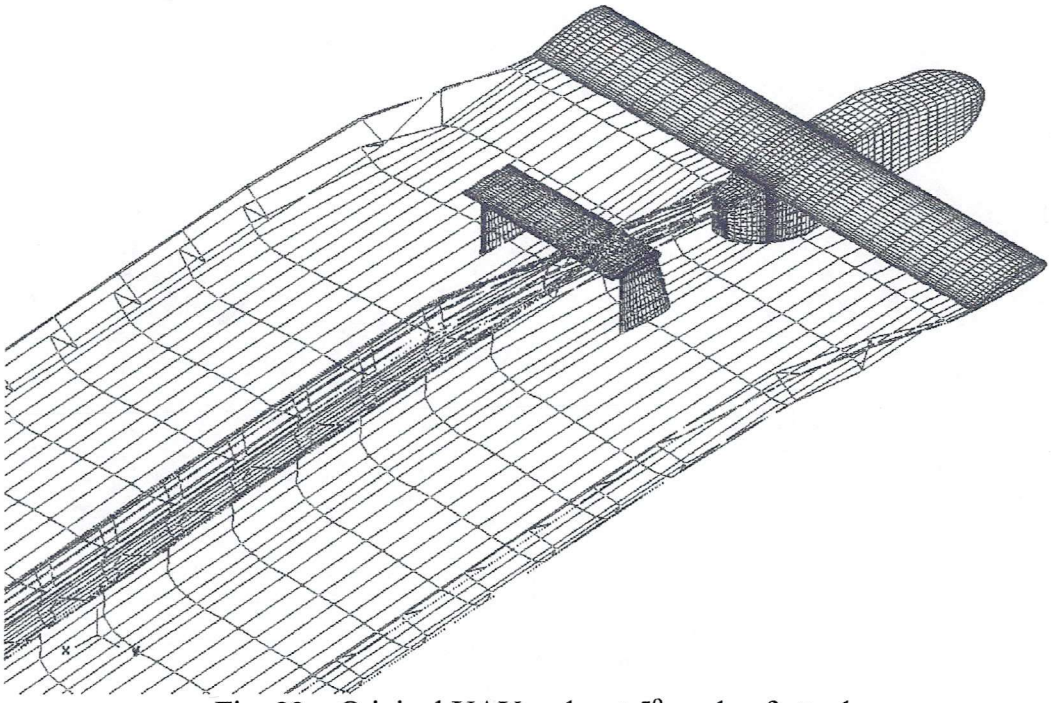

Fig. 23 – Original UAV wake at 5° angle of attack

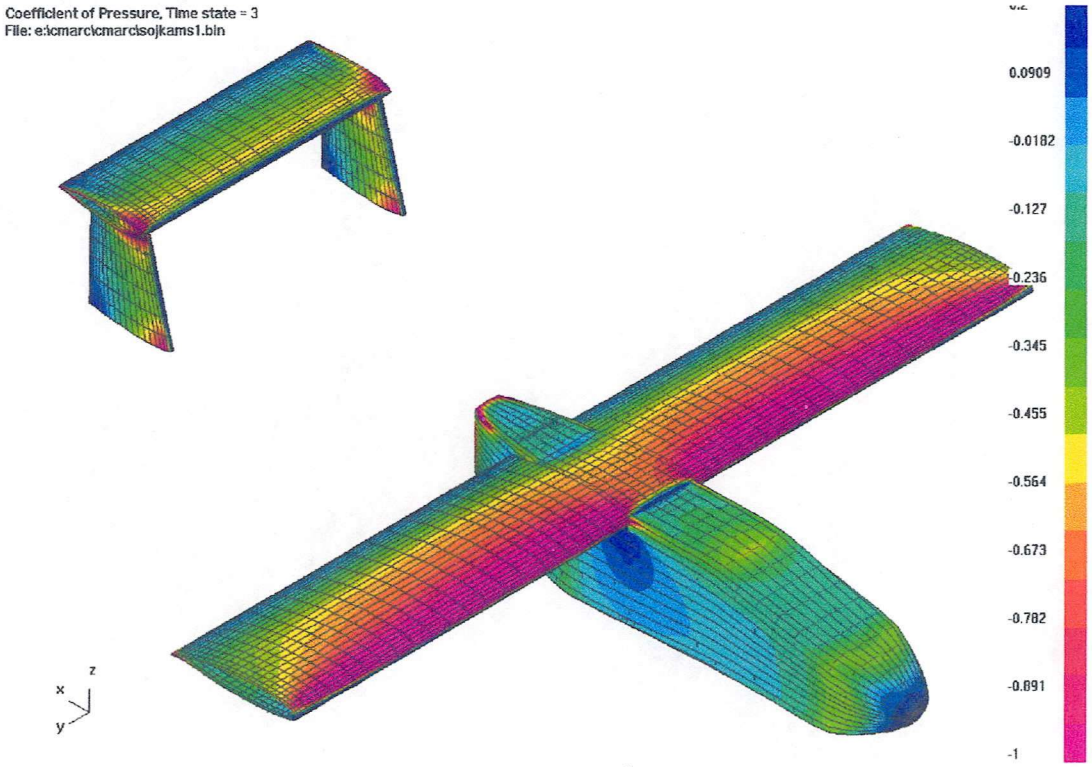

Fig. 24 - UAV MS 0313 at 5° angle of attack

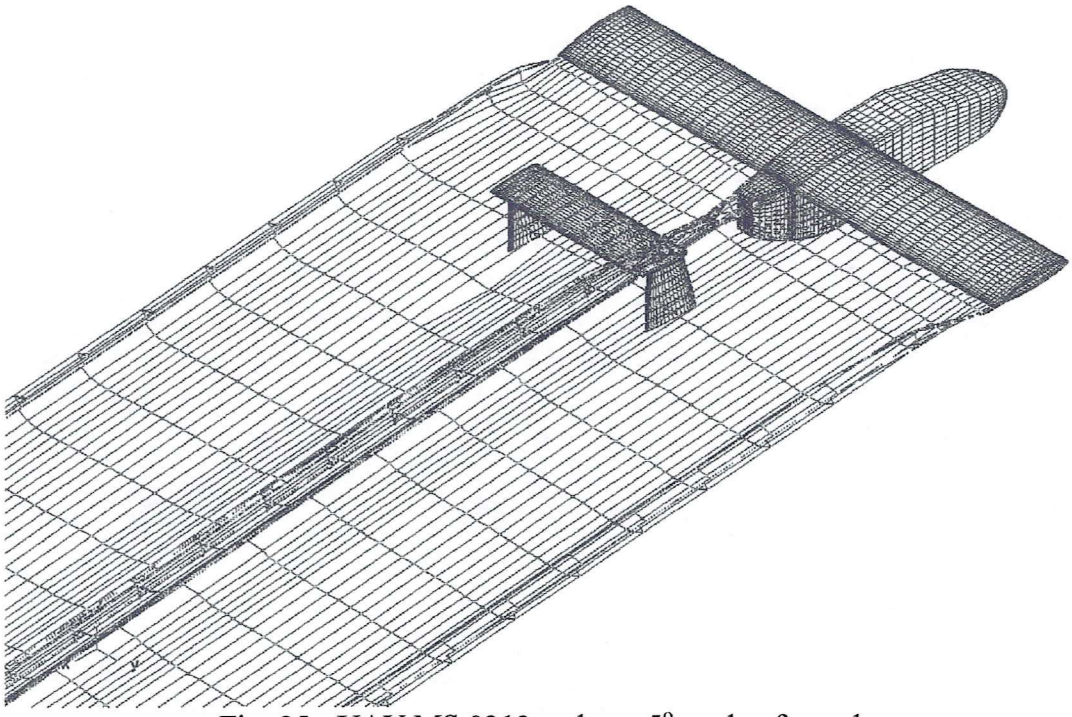

Fig. 25 - UAV MS 0313 wake at 5° angle of attack

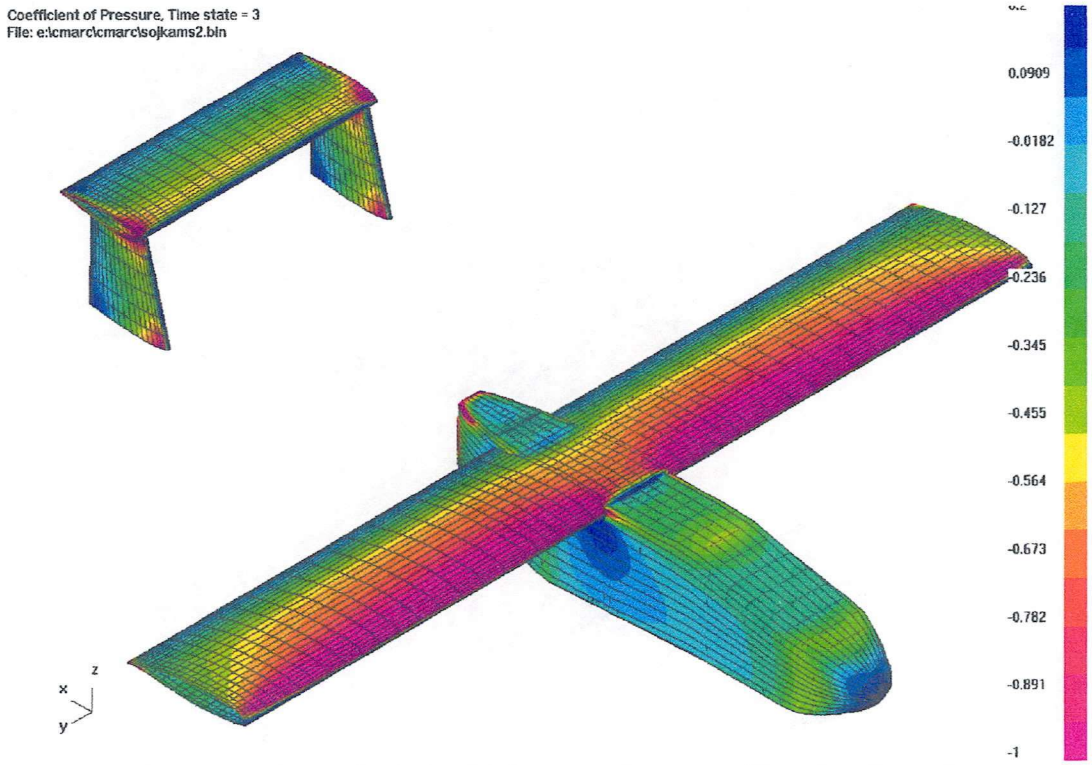

Fig. 26 - UAV MS 0313 with increased span at 5° angle of attack

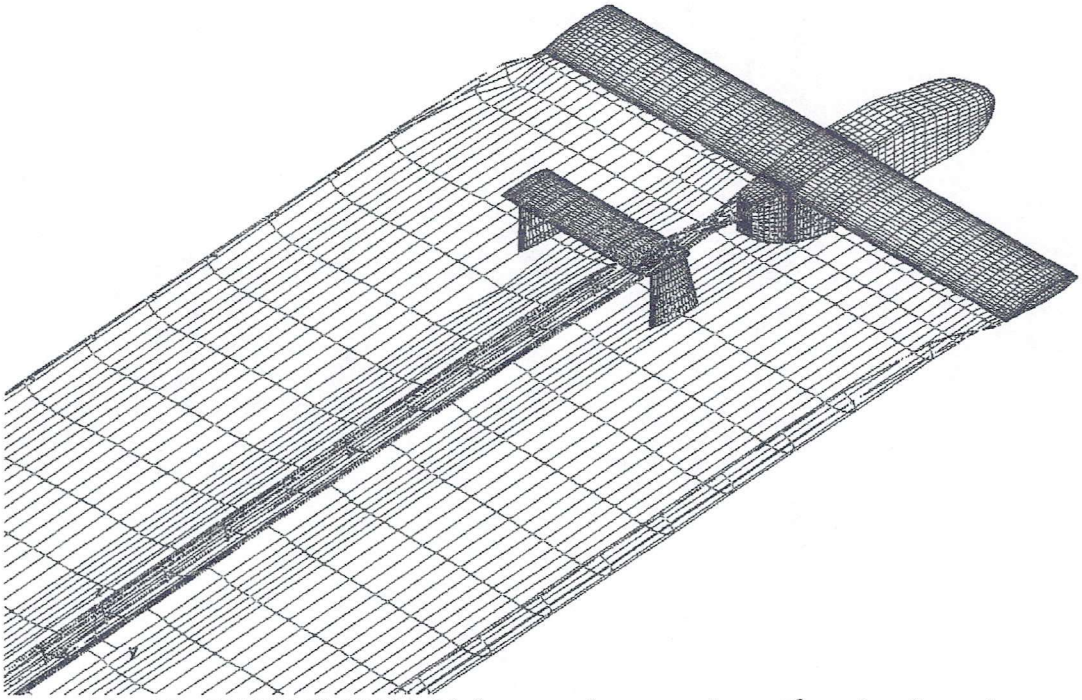

Fig. 27 - UAV MS 0313 with increased span wake at 5° angle of attack

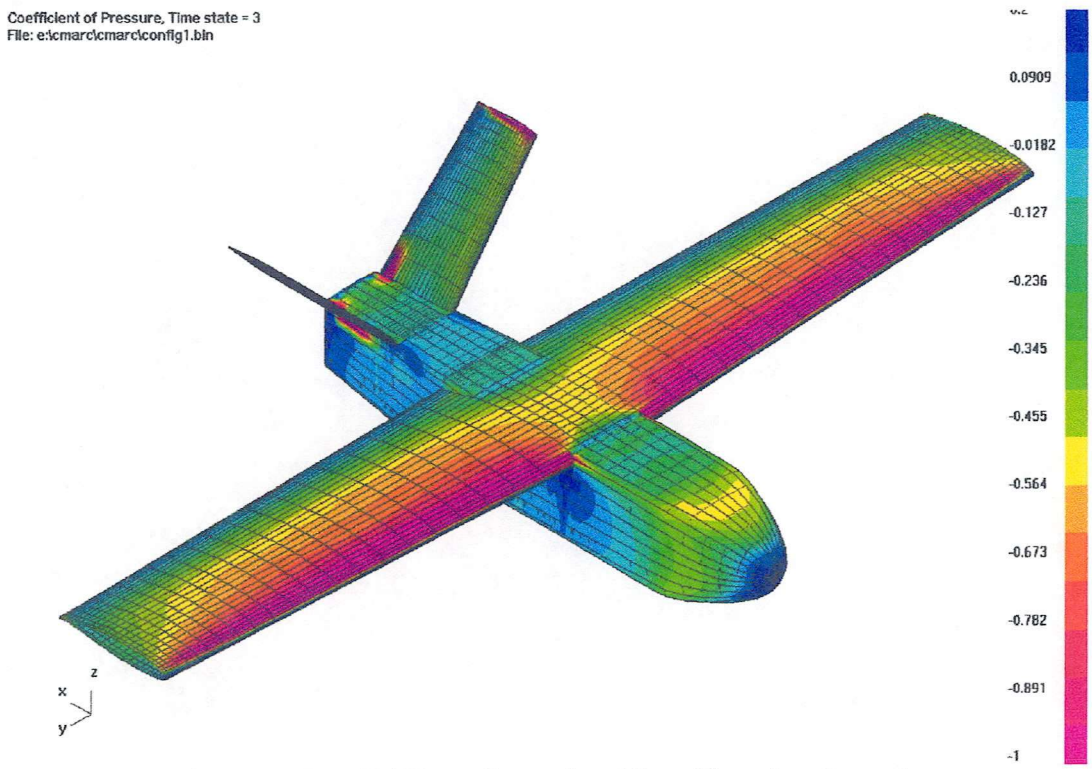

Fig. 28 - New UAV configuration (1) at 5° angle of attack

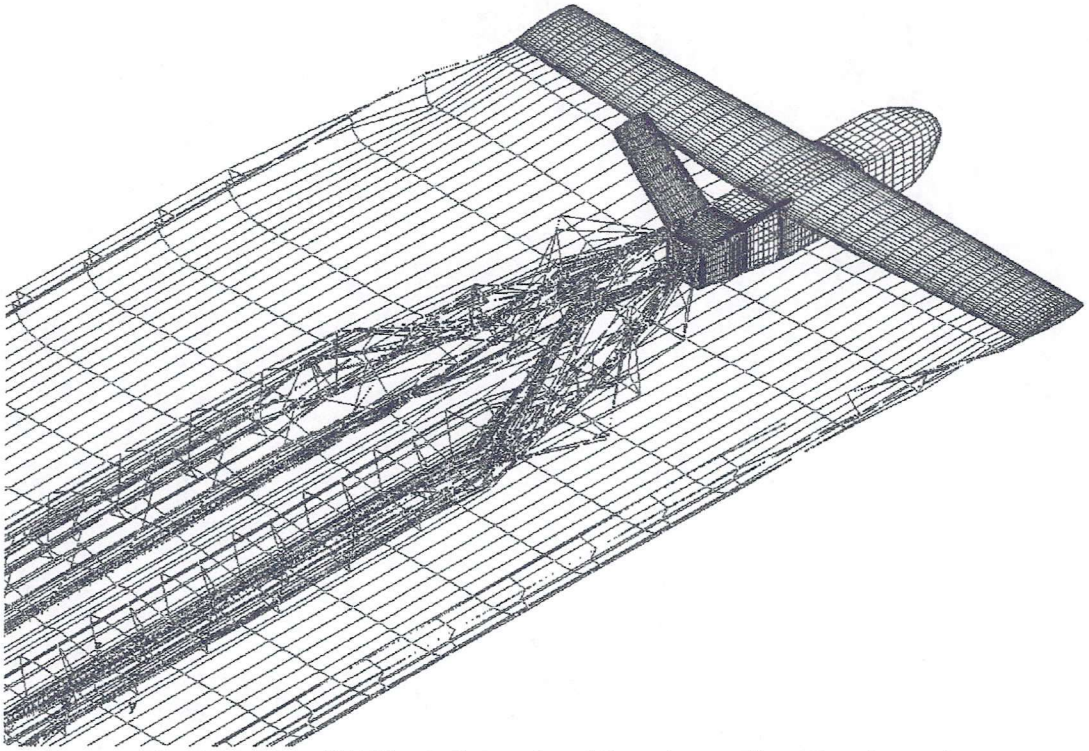

Fig. 29 - New UAV configuration (1) wake at 5° angle of attack

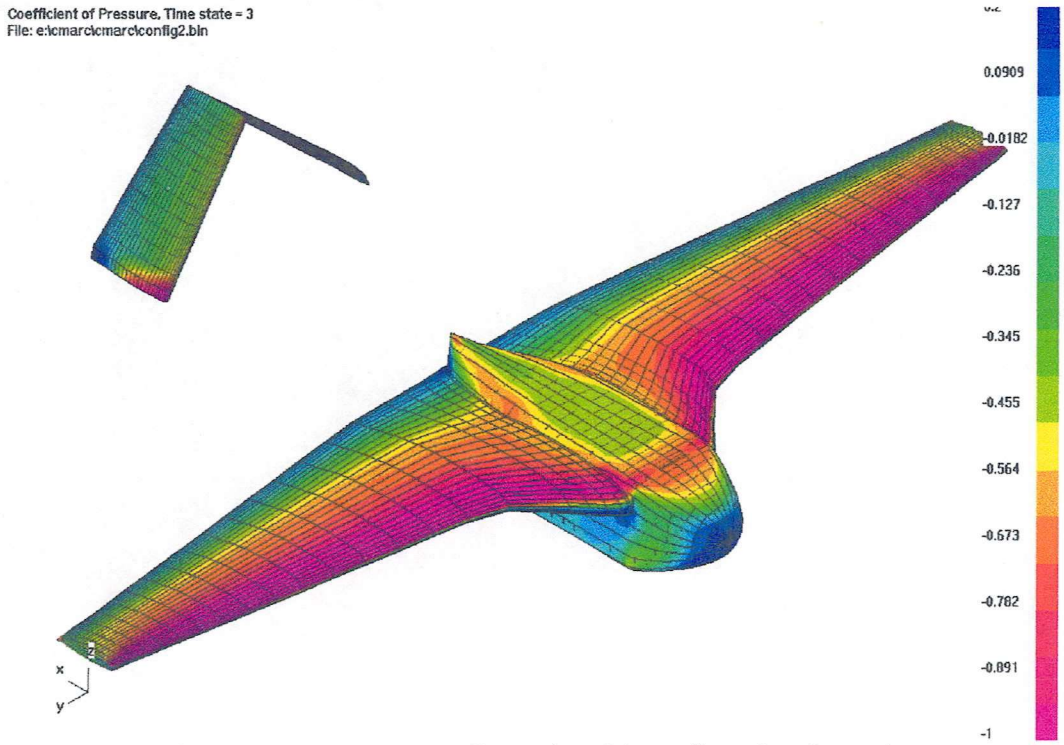

Fig. 30 - New UAV configuration (2) at 5° angle of attack

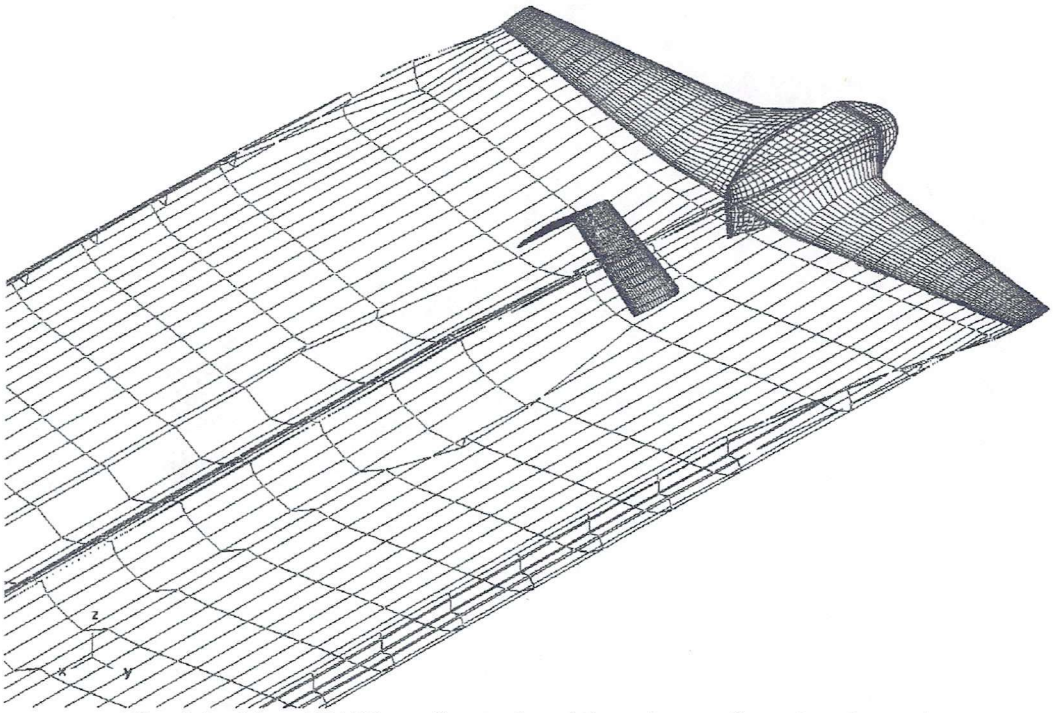

Fig. 31 - New UAV configuration (2) wake at 5° angle of attack

6.3 CONFIGURATIONS AT 10° ANGLE OF ATTACK

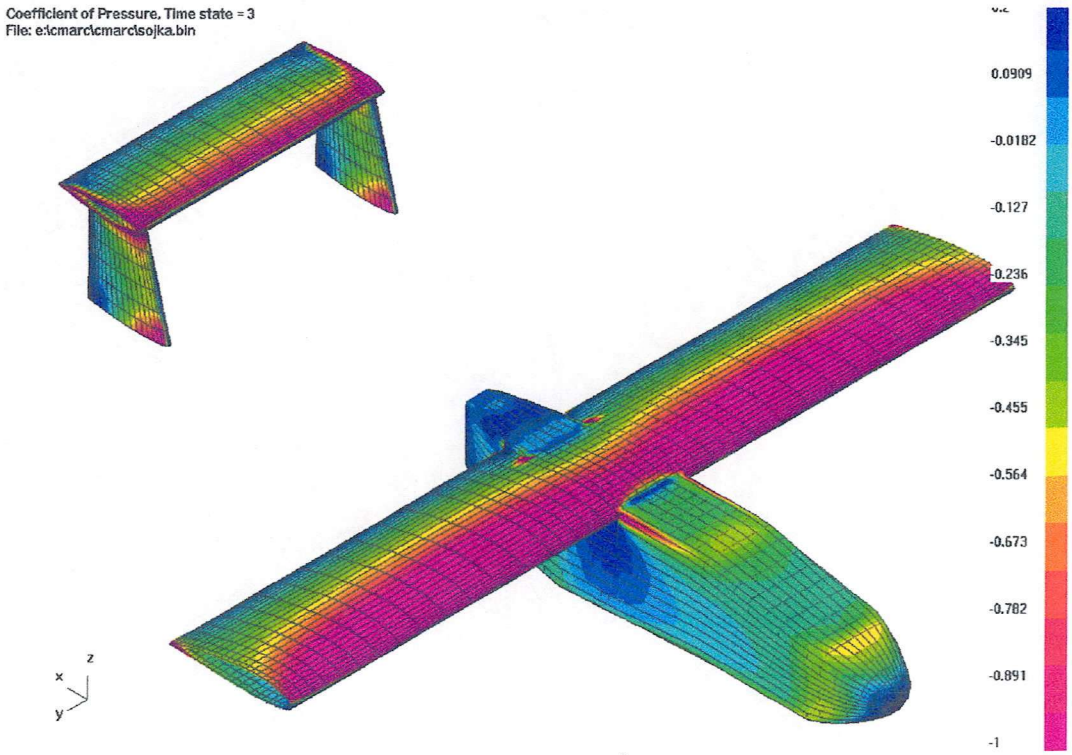

Fig. 32 – Original UAV at 10° angle of attack

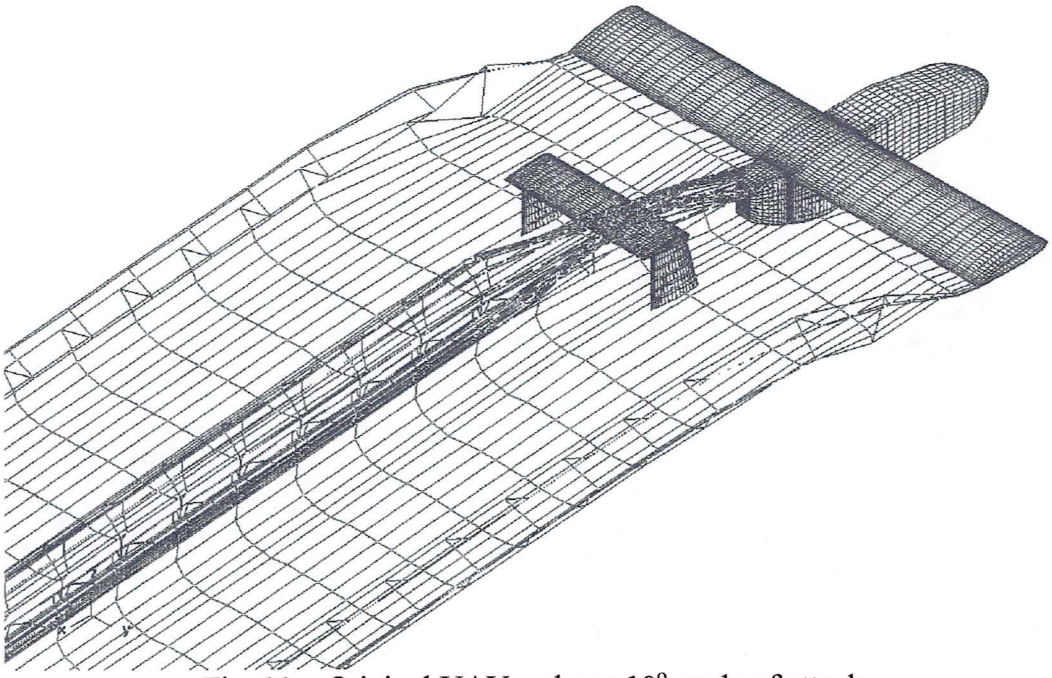

Fig. 33 – Original UAV wake at 10° angle of attack

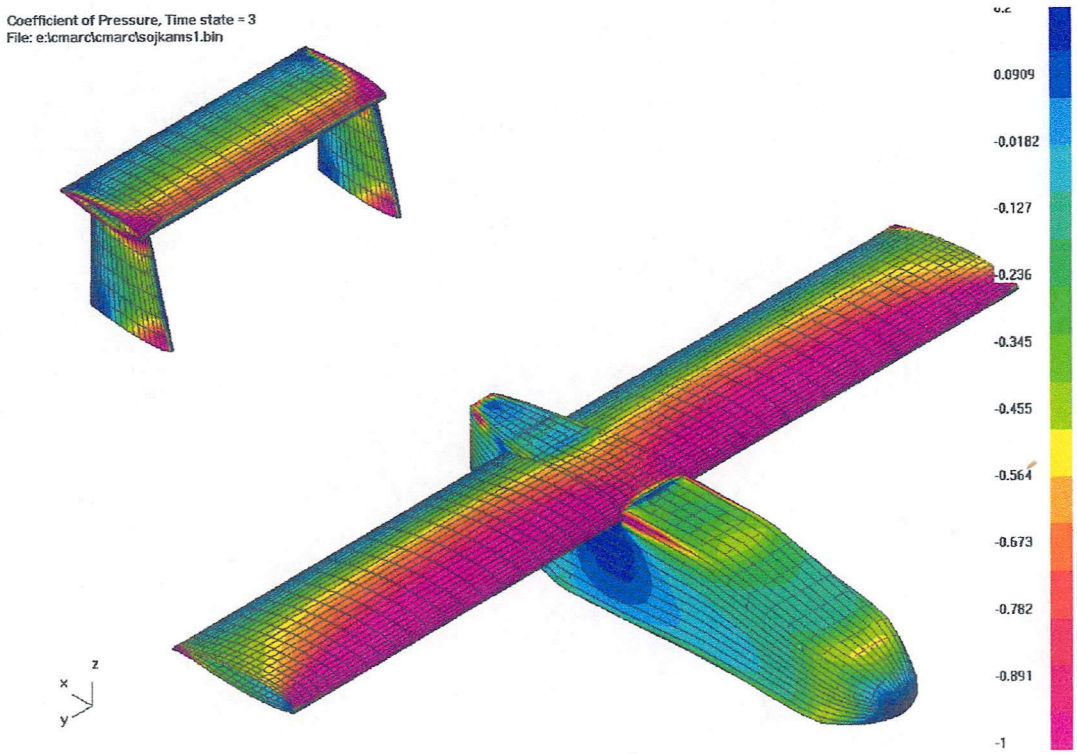

Fig. 34 - UAV MS 0313 at 10° angle of attack

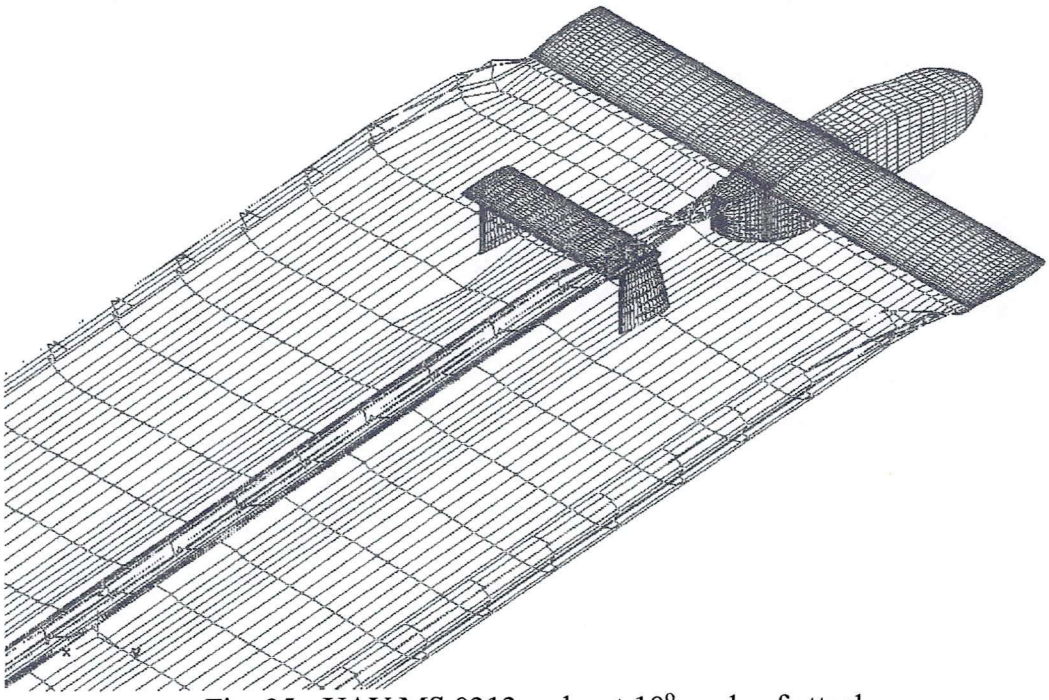

Fig. 35 - UAV MS 0313 wake at 10° angle of attack

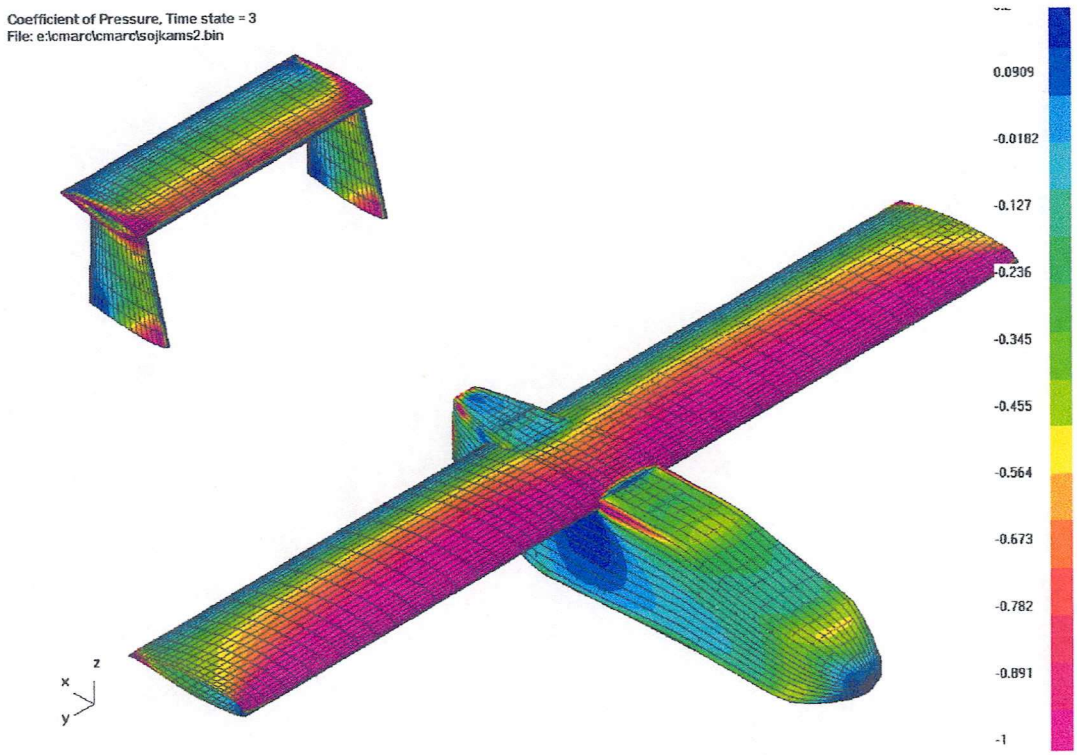

Fig. 36 - UAV MS 0313 with increased span at 10° angle of attack

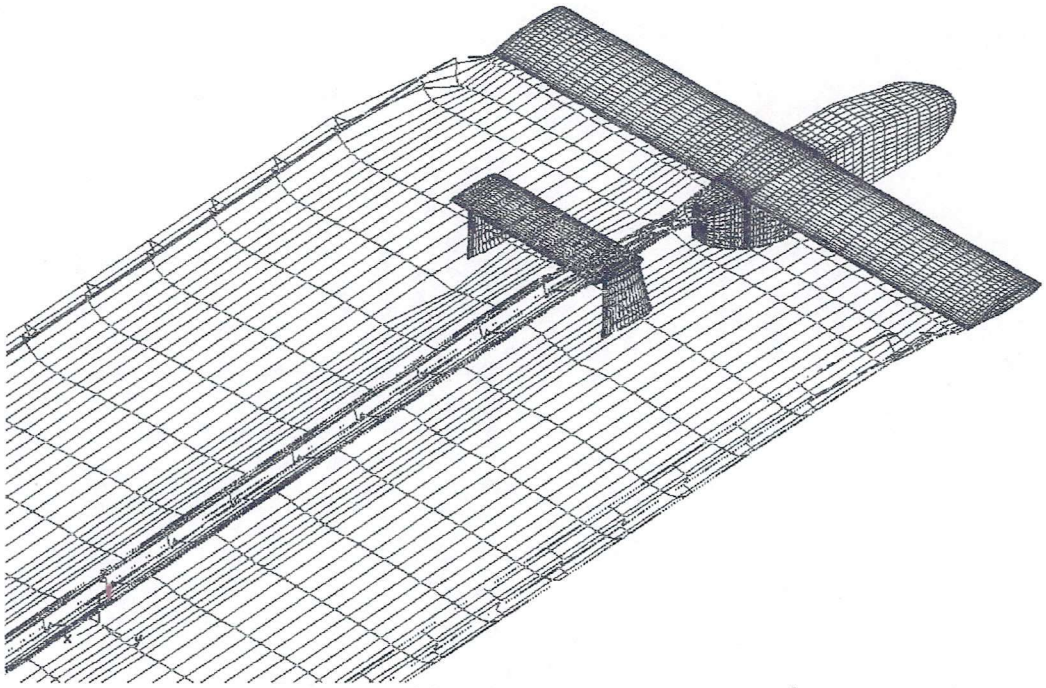

Fig. 37 - UAV MS 0313 with increased span wake at 10° angle of attack

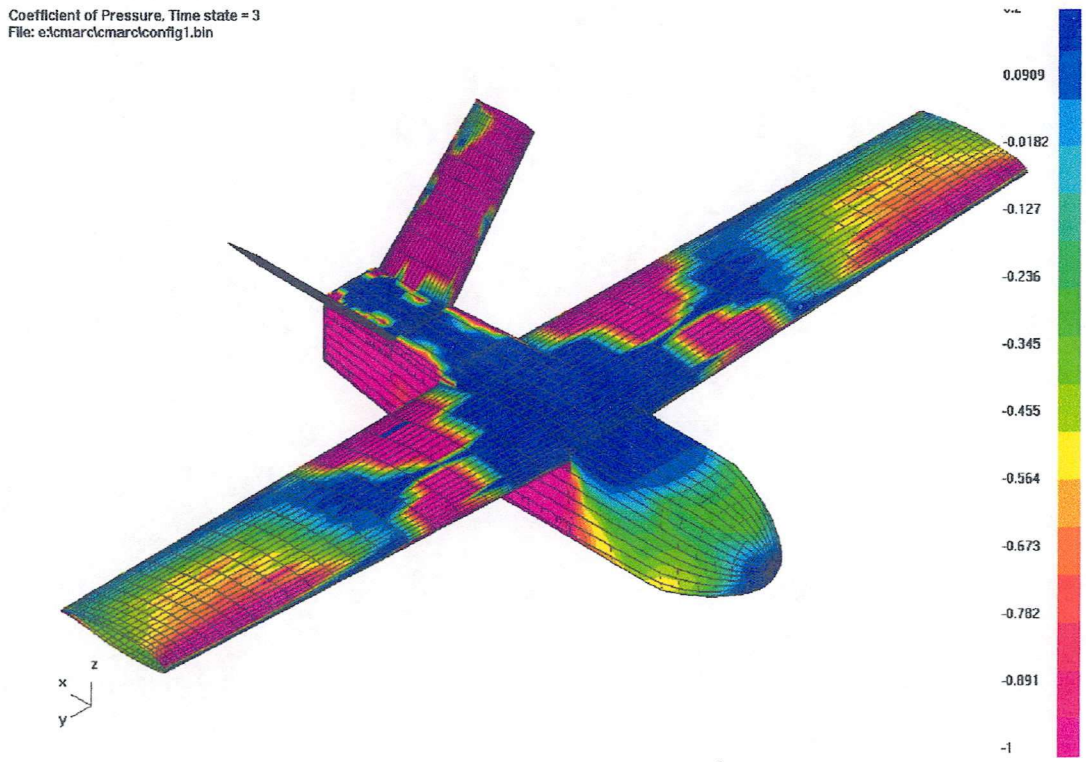

Fig. 38 - New UAV configuration (1) at 10° angle of attack

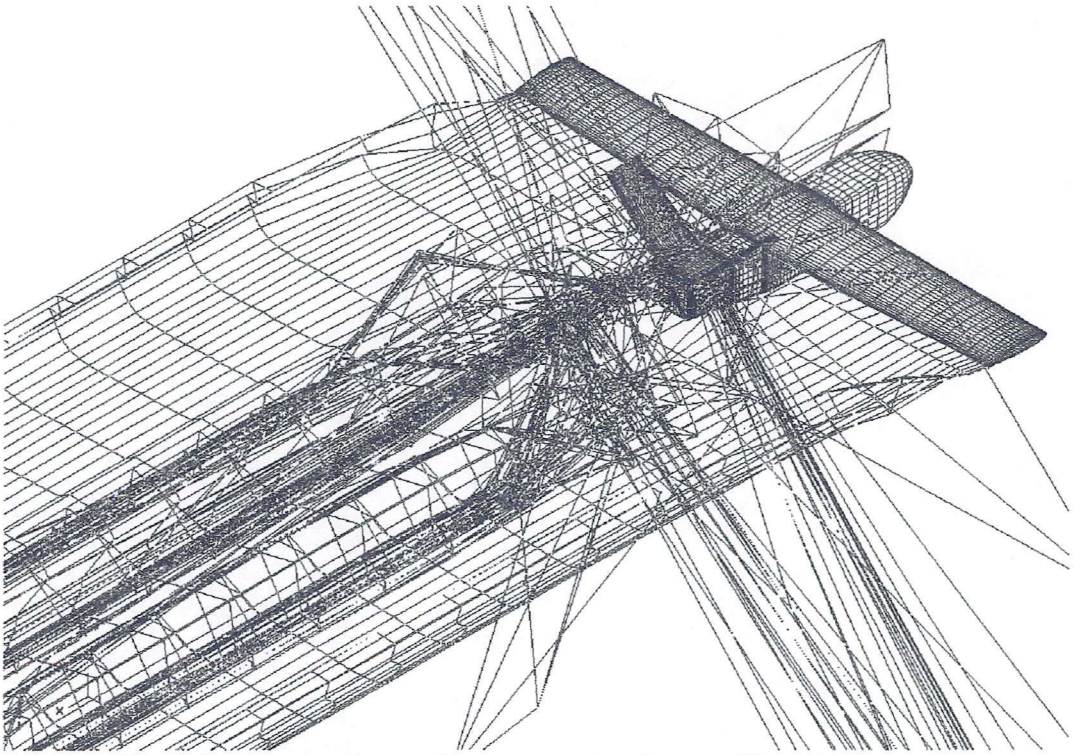

Fig. 39 - New UAV configuration (1) wake at 10° angle of attack

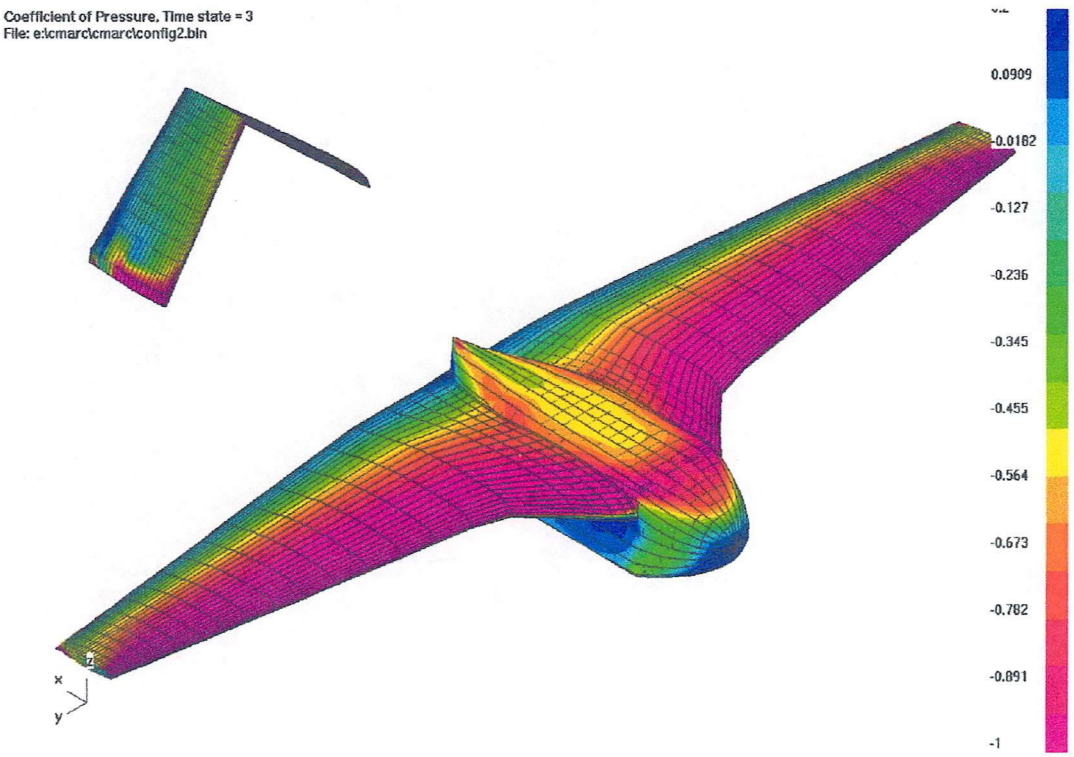

Fig. 40 - New UAV configuration (2) at 10° angle of attack

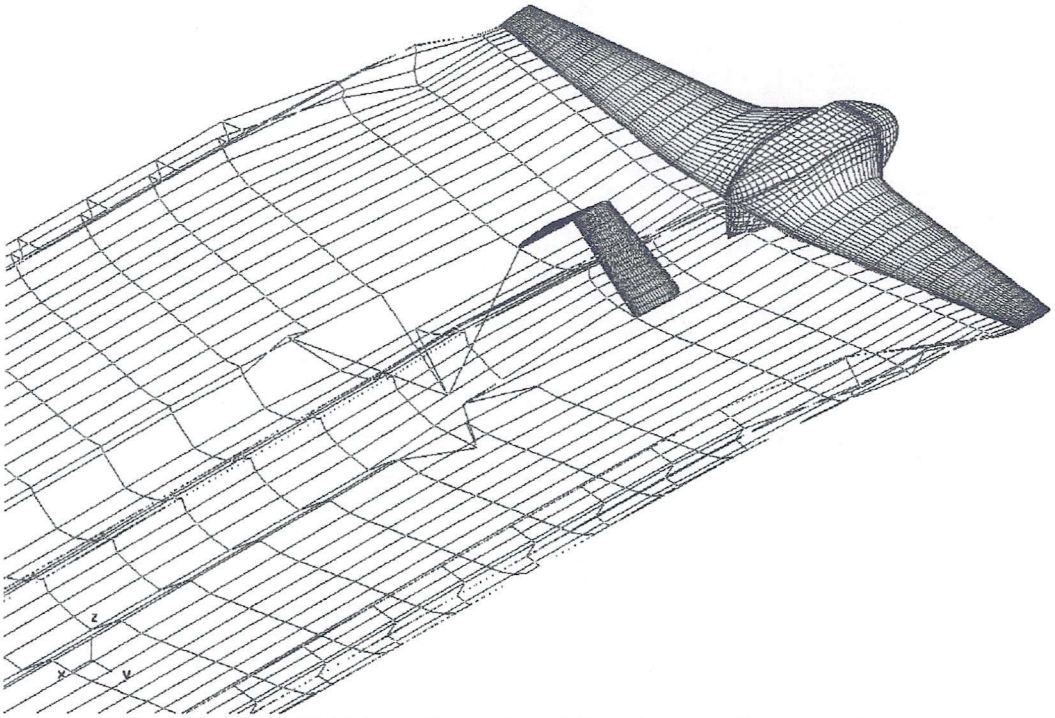

Fig. 41 - New UAV configuration (2) wake at 10° angle of attack

6.4 CONFIGURATIONS AT -5° ANGLE OF ATTACK

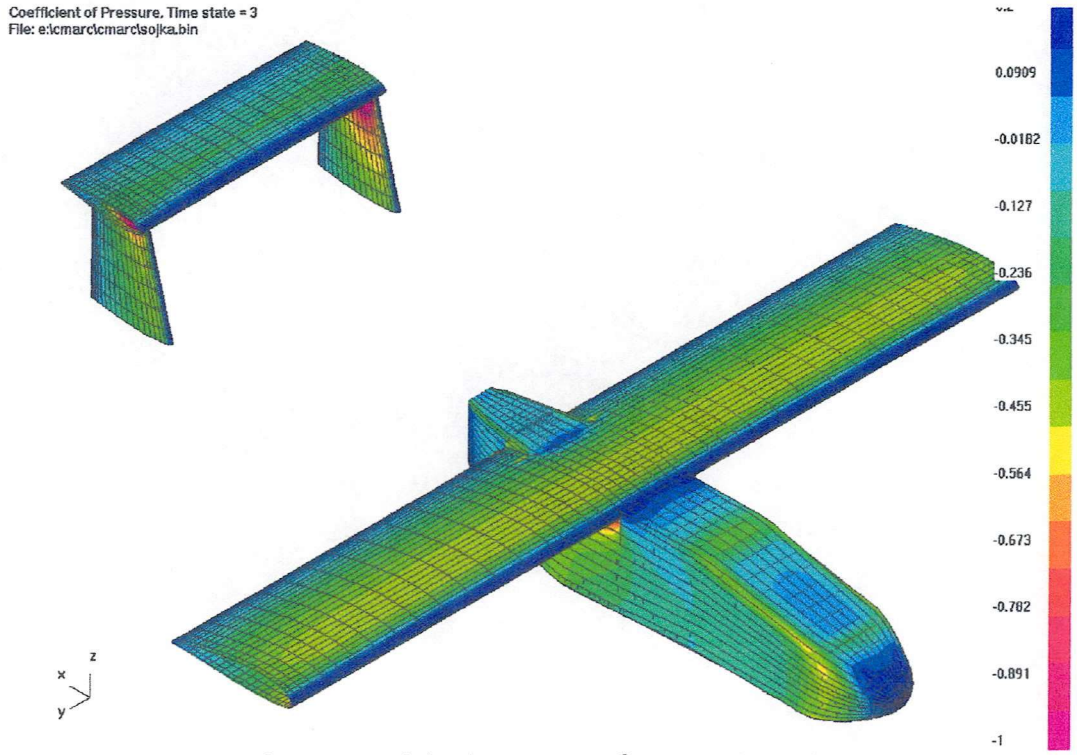

Fig. 42 – Original UAV at -5° angle of attack

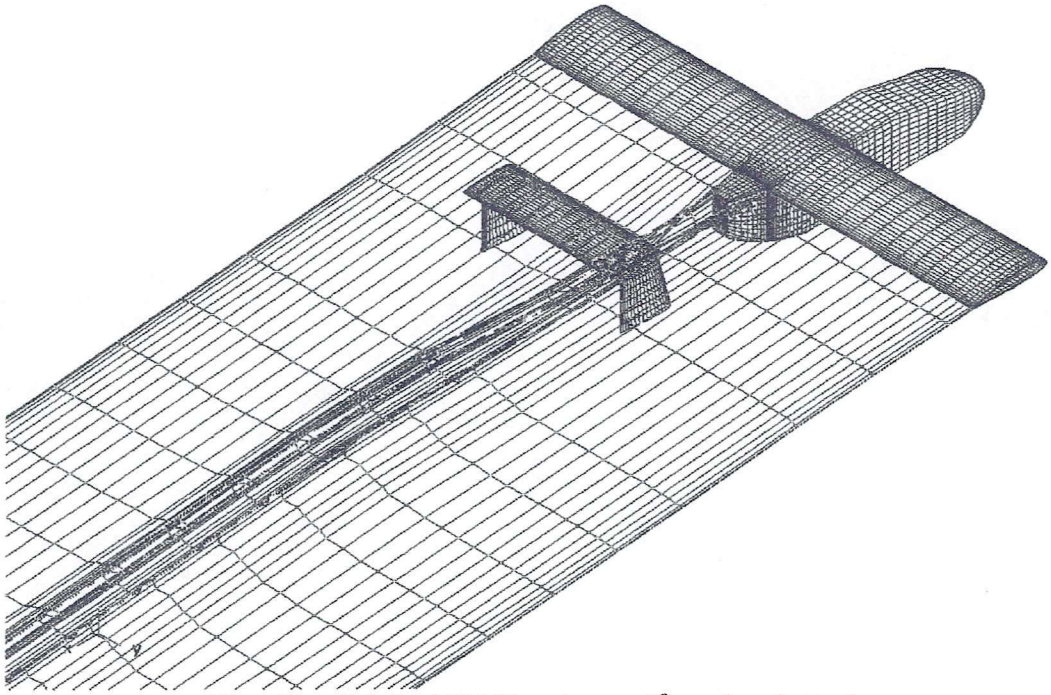

Fig. 43 – Original UAV wake at -5° angle of attack

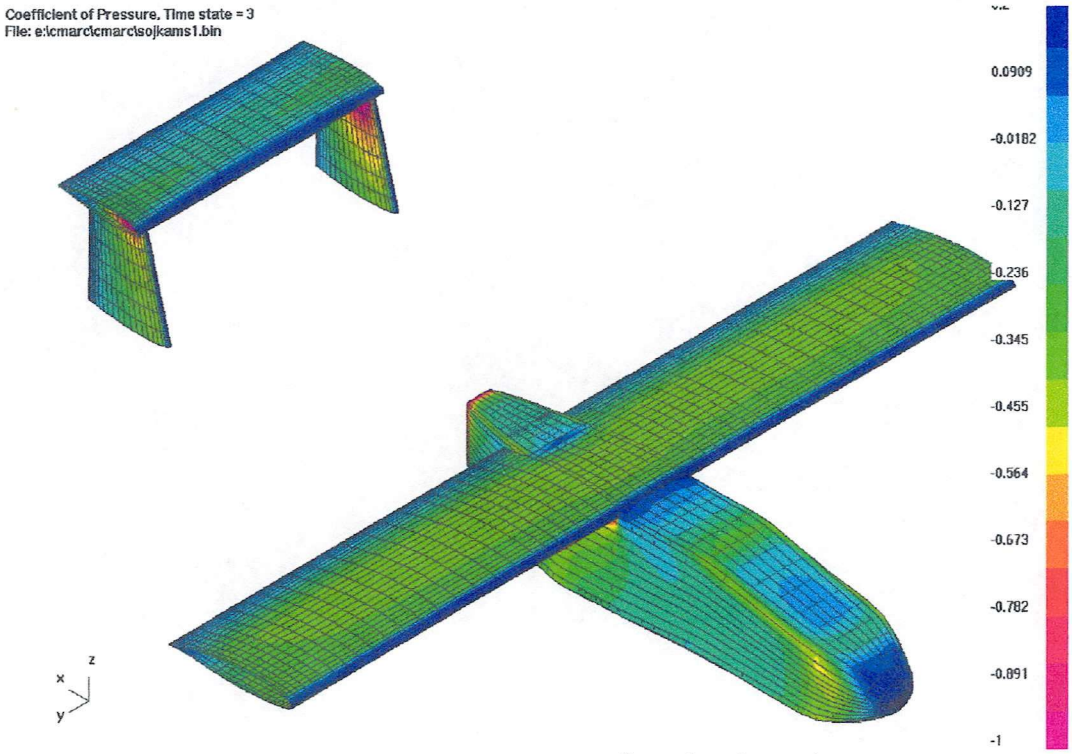

Fig. 44 - UAV MS 0313 at -5° angle of attack

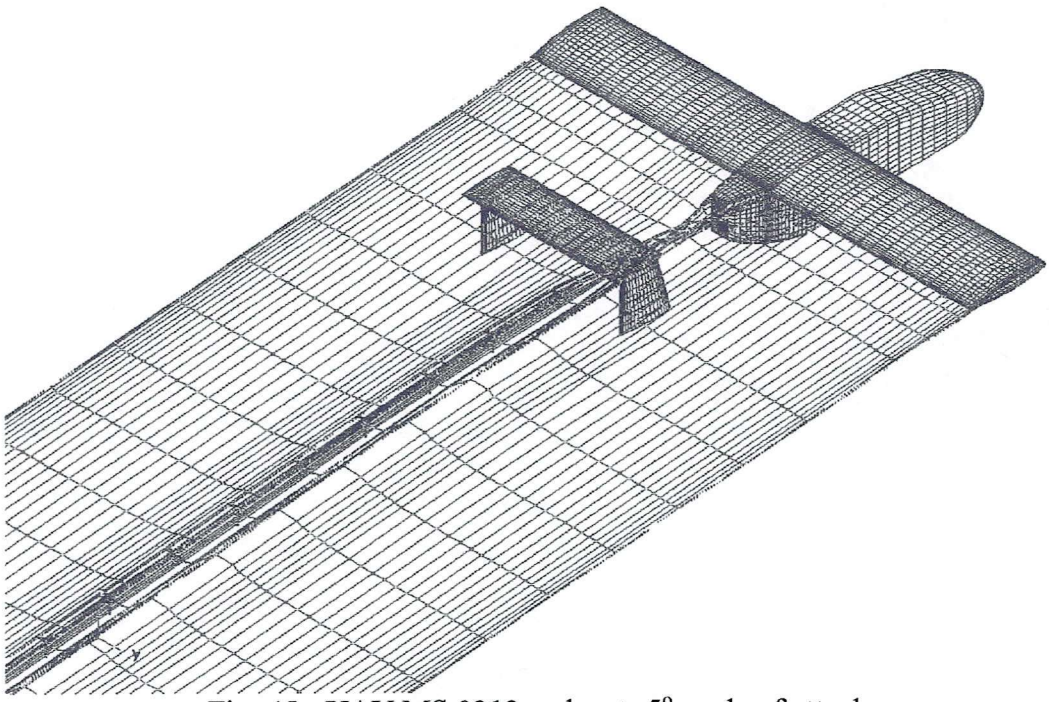

Fig. 45 - UAV MS 0313 wake at -5° angle of attack

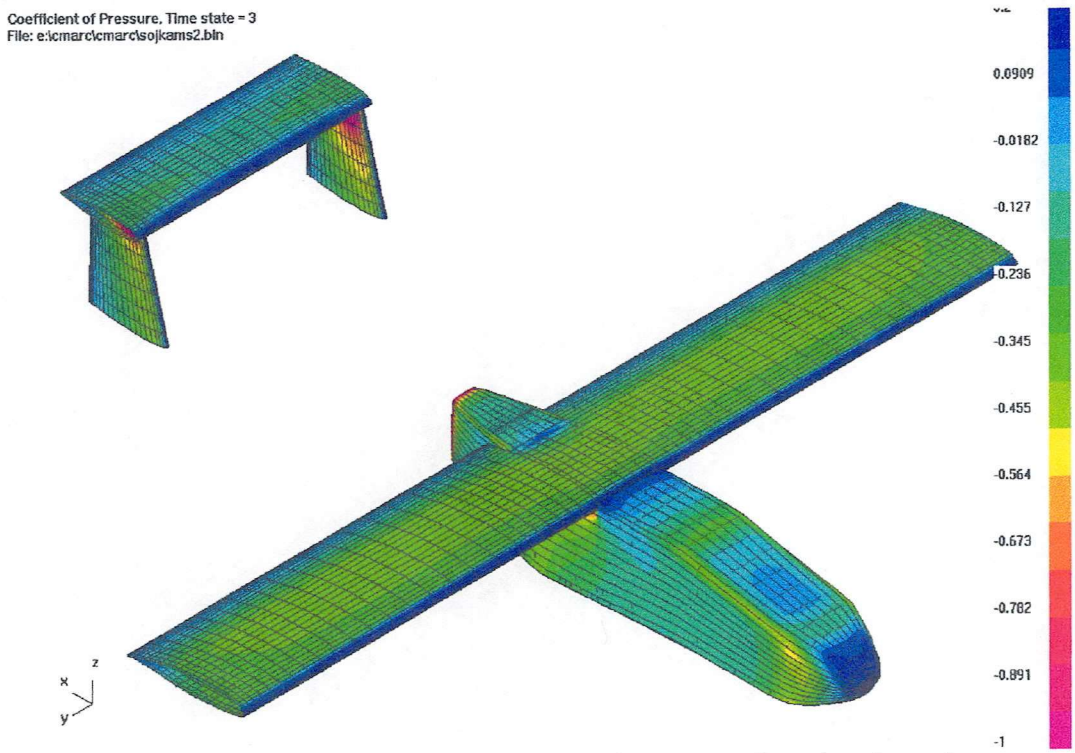

Fig. 46 - UAV MS 0313 with increased span at -5° angle of attack

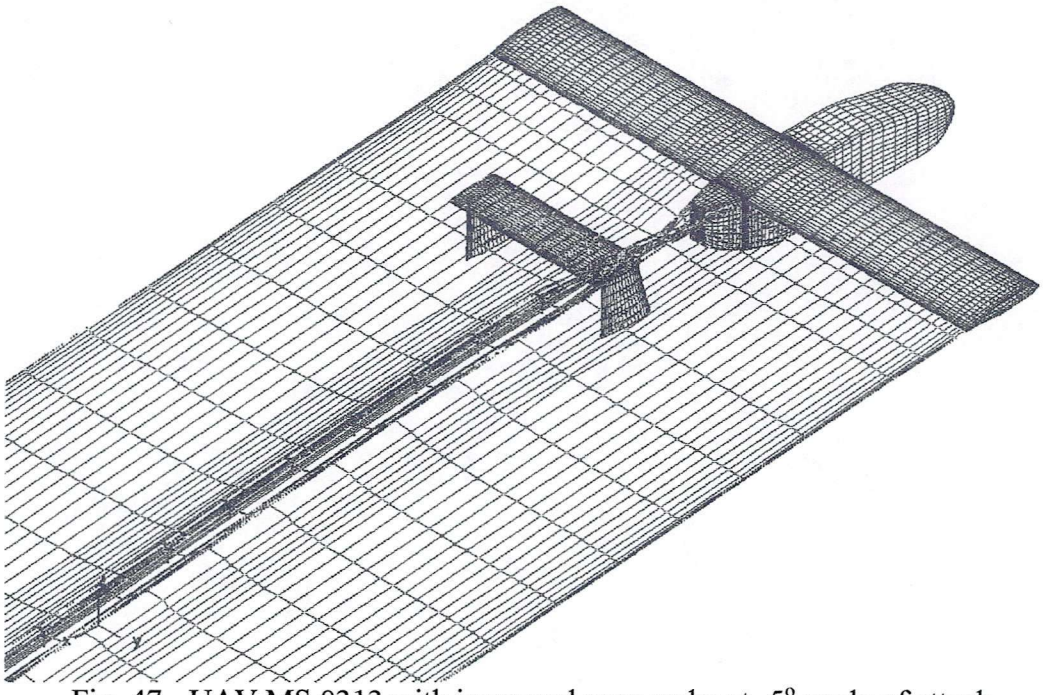

Fig. 47 - UAV MS 0313 with increased span wake at -5° angle of attack

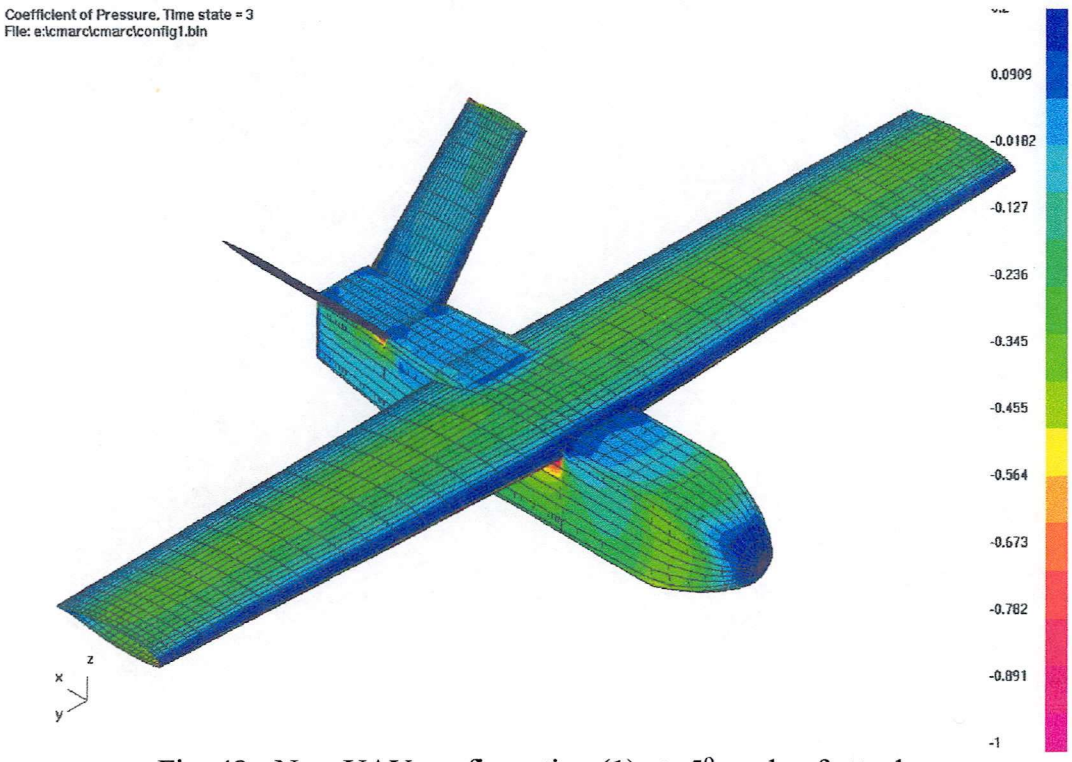

Fig. 48 - New UAV configuration (1) at -5° angle of attack

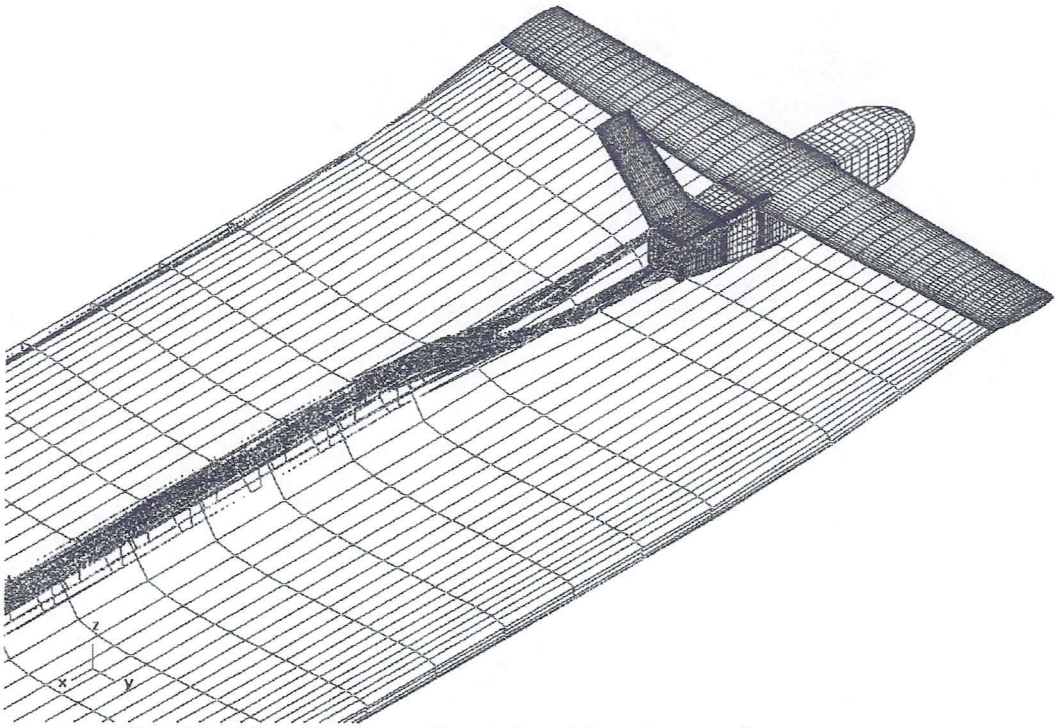

Fig. 49 - New UAV configuration (1) wake at -5° angle of attack

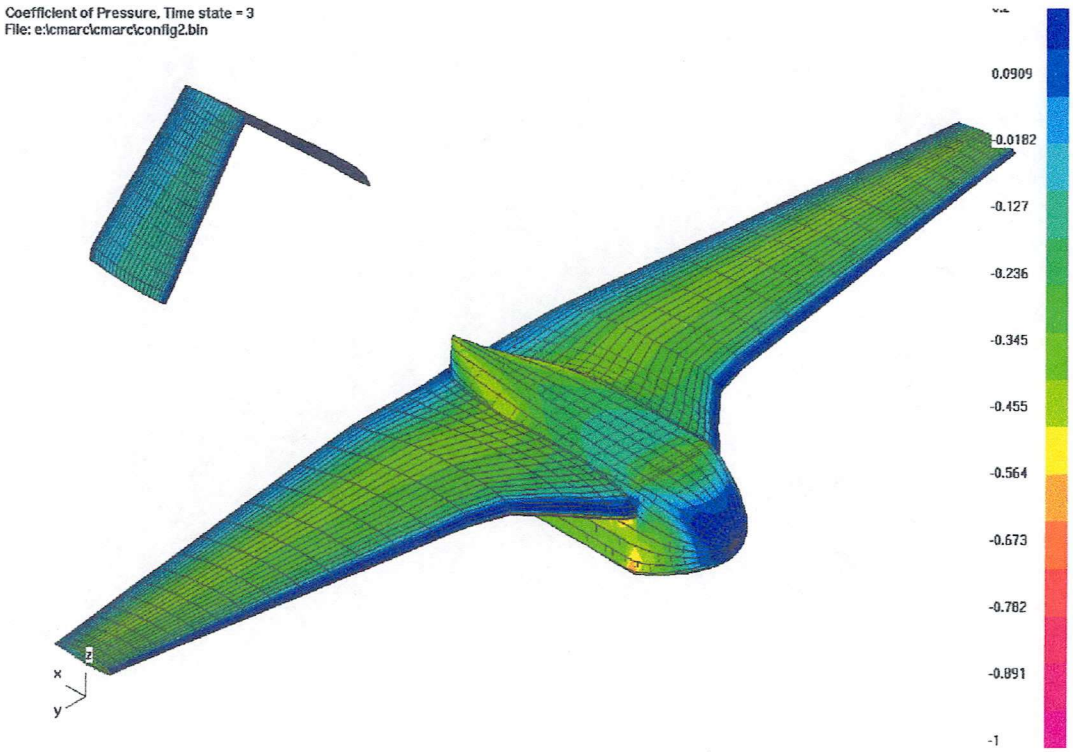

Fig. 50 - New UAV configuration (2) at -5° angle of attack

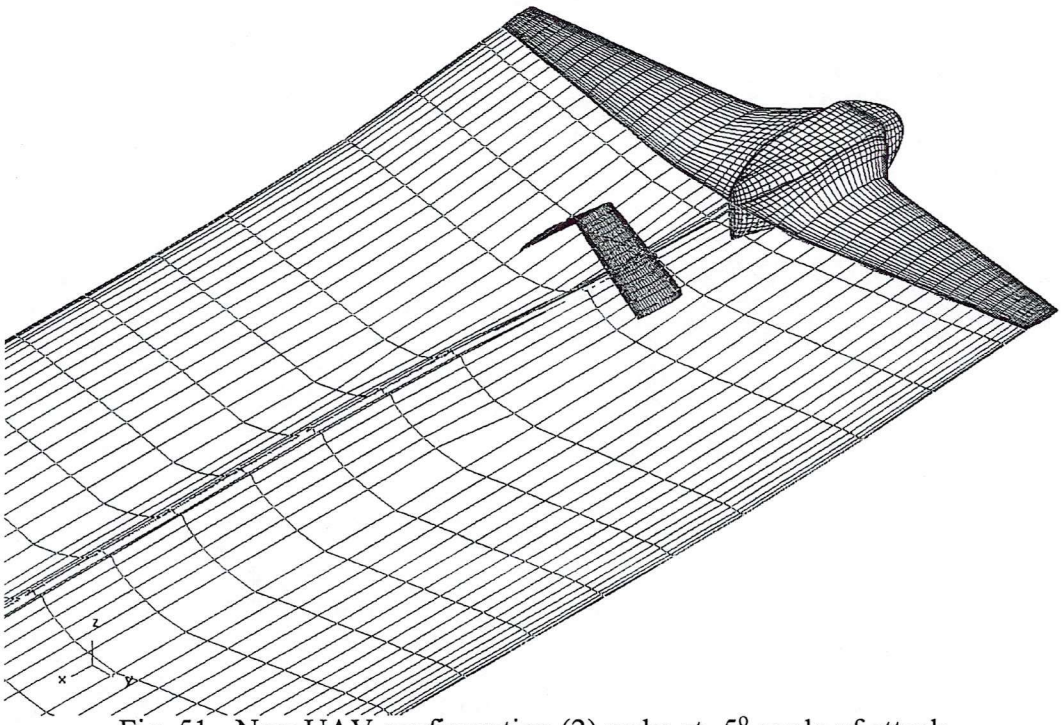

Fig. 51 - New UAV configuration (2) wake at -5° angle of attack

6.5 DRAG POLARS AND LIFT CURVES

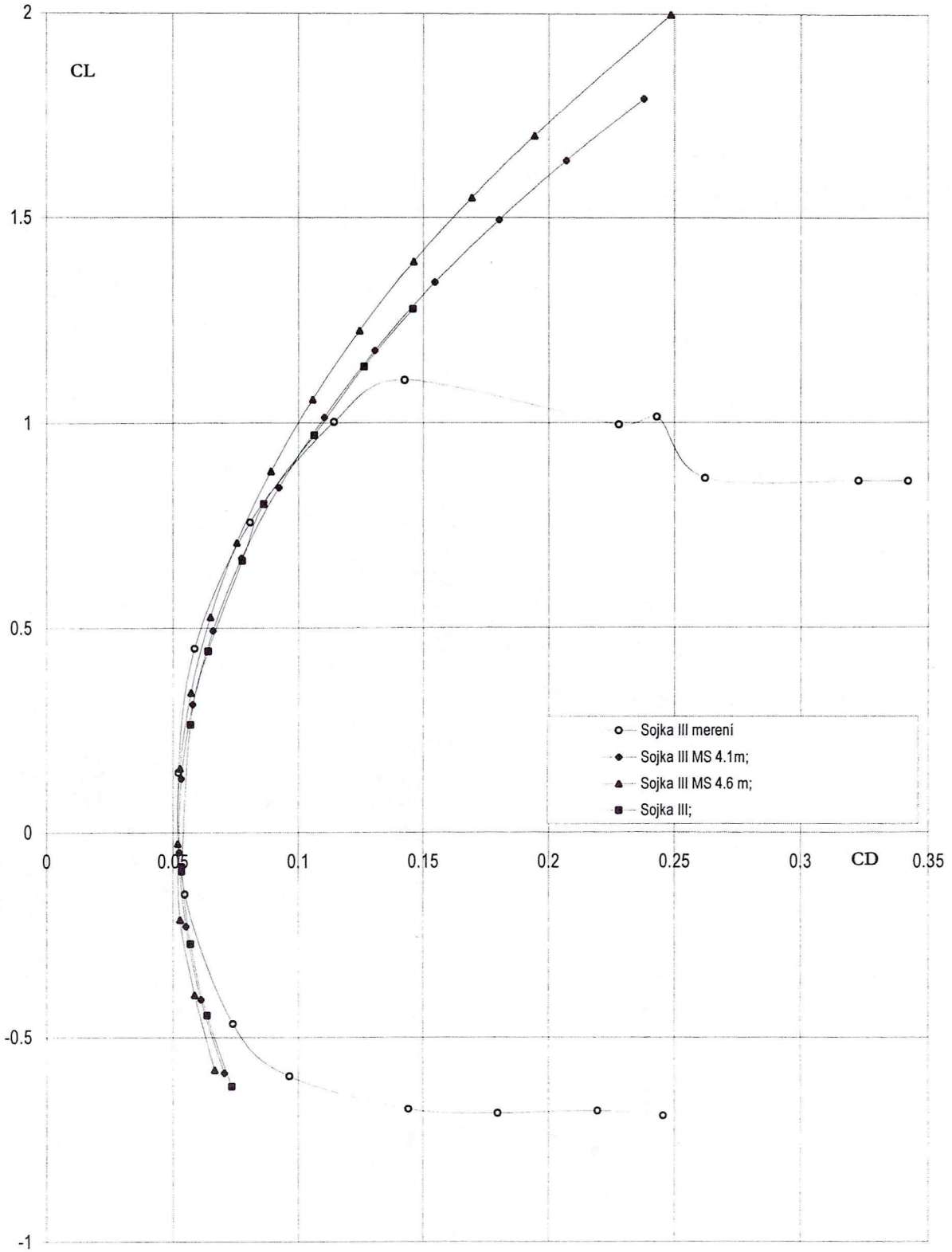

Fig. 52 – Drag Polar Curves

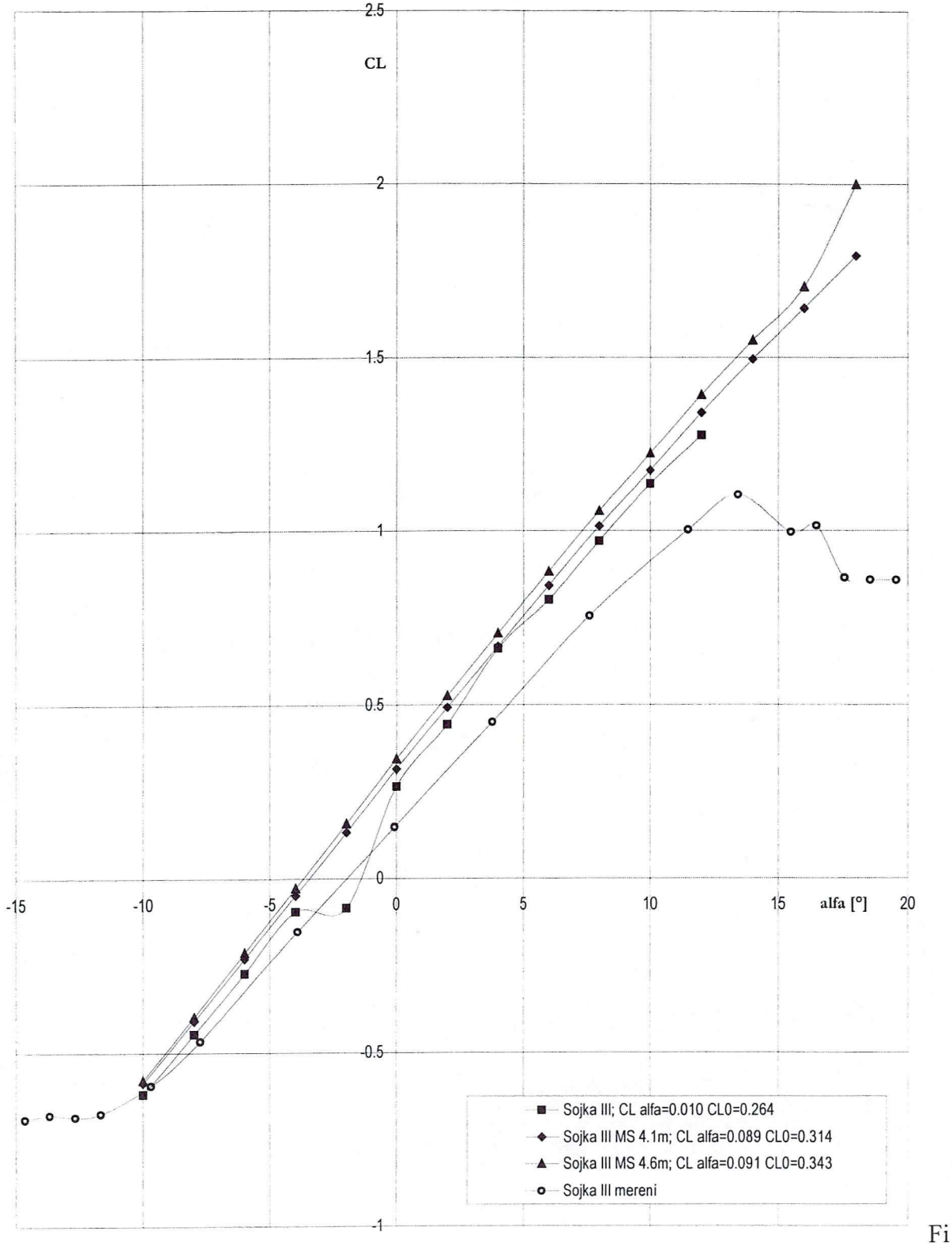

Fi

g. 53 – Lift Curve Slopes

Figs. 52 and 53 show the drag polars and lift curves for the first 3 UAV configurations analysed.

Once again it is worth pointing out here that the analysis was done under invisicid conditions, so theoretically no drag values were obtained form the analysis. In order to obtain the drag values hand calculations were done. Only 3 of the configurations were looked at this stage, the results obtained for the new configurations were a little suspicious to say the least. In particular the new configuration (1), which seemed to breakdown quite early in the analysis, though the configuration (2) did seem to hold together quite well and fair slightly better in producing viable results.

7. DISCUSSION

7.1 CONFIGURATIONS AT 0° ANGLE OF ATTACK

Firstly, there is the original UAV model. Fig. 12 shows the pressure coefficient plot for this configuration at 0° angle of attack with no yaw.
From the scale on the right hand side of the picture, it can be noticed that the blue and colder colours depict the higher pressures and the lower pressures are depicted by reds and violets, the warmer colours. Furthermore it can be said that the higher pressures denote areas of slow moving flow and low pressures regions of faster moving flow.

Surveying fig. 12 above we notice several aspects typically expected on any conventional aircraft. Firstly, clearly visible are the large stagnation regions on the front of the nose and on the leading edge of the wings and horizontal tail. The extremely low, suction pressures are of course situated on the upper surface of the wing at the point of maximum camber. The effect is altered slightly by the presence of the fuselage and the wing tips which see the region taper off. The remainder of most of the fuselage is experiencing moderate pressures. The stagnation point on the leading of the edge causes an effect on part of the fuselage underneath the wing and at the leading edge intersection point, coincidental with a large stagnation region on the upper surface of the fuselage at the wing/fuselage intersection. This phenomenon is mimicked on the horizontal tail. However, in this situation due to the nature of the section being symmetrical and the slight negative angle of attack the suction region is on the underside of the tail. This can be seen by the effect on the vertical fins of the tail.
Another point of note must be the relatively high pressures on the rear section of the fuselage and also the trailing edges of the lift producing surfaces. This is simply due to the modelling involved, which causes separation along the trailing edge. This is set a result of the inviscid nature of the program and so at consequent angles of attack these regions remain the same size and do not increase, as separation simply does not occur.

Meanwhile, fig. 13 shows the corresponding wake for the previous pressure coefficient plot. At this stage the wake really does not give much information away. The important features to note are the vortices from the fuselage and the wing tips, which are quite predominant.

The next pressure coefficient plot is of the UAV with the same set up as the previous configuration, although here the aerofoil section has been replaced with a differing section. Fig. 14 shows the results obtained. In many ways this plot is very similar to the aforementioned one, although there are clear differences. Easily distinguishable are the stagnation pressures on the fuselage nose, on the upper surface of the fuselage at the wing intersection, and their effect on the fuselage underneath the wing. The tails are virtually identical. The main discernible differences are the shape of the suction region on the upper surface of the wing and that of the rear of the fuselage. The change in shape of suction region is due of course to the change in profile, the region is thinner, though stretches right to the wing tips. It also has a higher pressure over the area of the fuselage intersection. This may also in some way be responsible for the reduction in pressures over the rear of the fuselage, in fact this can be the only explanation as nothing else but the wing section has changed. Indeed, very low pressures are visible right at the very rear edge of the fuselage, something that is not present in the original UAV configuration.

The ensuing wake plot, fig. 15, for this configuration and angle of attack at a first glance looks identical, though more in depth perusal reveals slight differences. The wake resulting

from the fuselage appears to be far smoother and less turbulent. The tip vortices also look improved, by saying that it is meant that they have a more characteristic tip vortex effect, with the outward streamline curving over more smoothly echoing the swirl seen on wingtips to a certain extent. All in all this produces a much more aesthetically pleasing wake.

The next pressure coefficient plot, fig. 16, shows the UAV with the new aerofoil section and with the additional factor of an increased span.
Despite the difference of the larger span, this pressure coefficient plot is almost identical to the previous case, and no real points of interest or difference can be raised. This in fact was a trend that was to continue throughout the analysis.

Fig. 18 shows an entirely new configuration of UAV, the tailbooms having been removed, the fuselage lengthened and a vee tail installed instead of the more conventional vertical tail fins with the horizontal tail resting on top. The ramifications for the model were that modelling became more straightforward and did not require any major simplifications, as was previously the case where the tail booms had to be ignored. The pressure coefficient plot however, seems to infer that this change in configuration causes major changes in the flow over this vehicular design. Some of the more common features are the high pressures on the nose and on the wing leading edge intersection with the fuselage. It should be noted here that the wings were set at 0^{o} as the wing angle of attack was to be determined. A huge aspect of deviation from the previous results is the lack of a sufficient suction region on the upper surface of the wing. Slightly lower pressures can be visible, but only over a small region, and this is an anomaly that seems to propagate aftwards, affecting the rear of the fuselage which shows irregular pressure patterns and also the vee tail, which looks slightly irregular though not completely abnormal.
Looking at the subsequent wake plot for the new configuration 1, fig. 19, consistent with the previous 2 results with the new aerofoil we see well formed tip vortices. However, the fuselage wake seems very distorted and irregular given the vehicle is in level flight.

Fig. 20 shows the pressure coefficient plot for the second new UAV configuration. This marks a return to the more conventional and indeed expected results. Although the unusual tail does seem to show evidence of certain irregularities. The nose of the fuselage has a larger region of high pressure, this is due mainly to the fact that this design has a slightly less rounded nose. The wings adopting a form of delta wing design show well defined suction regions on the wings upper surface, which is more predominant on the outer wing section. At the front of the fuselage there is evidence of vortices, possibly coming from the wing/fuselage intersection point. More vortex shedding can be seen by the low pressure region which begins ¾ back on the fuselage at the intersection with the wing and propagates towards the rear of the fuselage. These vortices most probably originate at the junction between the change in wing section. The tail is similar in some ways to the previous new configuration, except here the vee tail has been inverted, and the results do show some similarities. The exception being low and high pressure regions on the leading and trailing edges at the intersection where the tailbooms would have been.
The wake for this particular model, fig. 21, is probably the smoothest and best, this is in no doubt due in some part to the more pronounced tapering of the aft of the fuselage in stead of the flat blunt region on the previous 4 cases. The wake looks better and the tip vortices are well defined.

7.2 CONFIGURATIONS AT 5° ANGLE OF ATTACK

The next set or results shows the various configurations of UAV at an increased angle of attack of 5°. Any discrepancies in results will be more pronounced due to the more irregular flow over the vehicles.

Firstly, fig. 22 shows the original existing UAV design at the increased angle of attack. The forward section of the fuselage remains much the same as the 0° case, although the high pressure region on the nose has moved downwards slightly. A stronger influence can also be seen by the increase in the size of the region on the fuselage at the wing intersection. The suction region on the upper surface of the wing has increased in size, whilst still tapering over the region coincident with the fuselage, and has also become slightly more negative. Turning attention to the tail, it can be seen that the upper surface of the horizontal tail is beginning to get a slight suction region. Also, low pressure regions are becoming visible at the leading edge of the intersection with the vertical and horizontal tail. At the base of the vertical fin, a low pressure region can be seen on the leading edge, whilst a high pressure region is on the trailing edge. The rear of the fuselage is appearing to become exposed to higher pressures than before with a deepening of the blue visibly clear.
Studying the corresponding wake for this configuration, fig. 23, and comparing with the previous case at 0° angle of attack, we can see that the tip vortices for this wake are slightly larger and also tending to become irregular. The fuselage wake is also larger, it too is showing an inclination to breakdown by becoming slightly irregular.

Fig. 24 shows the UAV with the new aerofoil. Evident are the expected things such as the high pressure on the nose, influence of the wing on the fuselage and moderate pressures on the fuselage body. The wing has a slightly differing pressure distribution than before due to the alternate aerofoil section employed, the overall suction region is about the same size, though the region of the really negative values is slightly smaller and is more pointed at the wing tips. This would tend to suggest that less lift would be generated. The tail is much the same as anticipated. Though there is a suggestion that the main body of the vehicle is having more of an influence on the tail as the pressures on the upper surface of the horizontal tail are more positive than with the original UAV at the same angle of attack. Though in every way such as at the vertical fin and horizontal tail intersections the low pressures are again present at the tail, along with the high pressures indicating separation.
The wake associated with the above configuration can be seen in fig. 25. Contrasting with the previous configuration it can be seen that this wake is much smoother and more organised, it follows on from what would be expected. The tip vortices are nicely formed and the fuselage wake shows little in the way of irregularities, indicating that this is a well modelled wake. Drawing parallels with the same configuration at 0° angle of attack this is simply following the trend of a well defined wake. In principle this should mean the model is quite sound and will provide good results before the wake calculations breakdown rendering any further analysis impossible.

Following on from the preceding configuration, fig. 26 shows the UAV with the new aerofoil and increased wingspan and as would be expected under such circumstances, there's very little difference between the previous configuration and this one. Everything is relatively identical with the exception that the wingspan has been increased.
The wake allied to this configuration is displayed in fig. 27, it shows similar trends yet again with the configuration before – smooth, well defined tip vortices and a well organised wake in general.

The first of the two new UAV configurations is shown in fig. 28. The problems of the 0° angle of attack seem to have continued into the 5° angle of attack, and indeed this increased angle of attack seems to have exacerbated them. Forward of the wing leading edge, the fuselage would appear to be relatively normal. From the wing leading aftwards little seems to be right, there is no smoothness to the regions of various pressures on the model, the suction regions of the wing are present but very irregularly shaped. The wing influence on the fuselage is even more irregular as is the tail region, which seems to be a bizarre mix or high and low pressures in unexpected places.
The wake, in fig. 29, bears witness to the oddity of the results obtained. The wake is very abnormal and on the point of breaking down completely, the tip vortices are very odd and the fuselage wake seems very haphazard in comparison with previous results, it is almost as if the angle of attack were higher than indicated. In passing comment, at this point it could be said that gaining results of this type is of no real use and serves no real purpose.

The second of the new configurations, fig. 30, on the other hand provides some rather pleasing results, at least everything is smoother and in the places where they are expected to be. High pressure on the nose, large suction areas on the wing, evidence still of vortices over the front of the fuselage which cannot be explained, along with vortex shedding at he rear of the fuselage that can be explained. The tail meanwhile is very plain, though the regions of high and low pressure on the tips intersecting where the tailbooms would be are growing.
The wake in fig. 31 is very clean and smooth, the tip vortices are a nice shape and the fuselage produces very little in the way of a disturbance in the flow. One abnormality in the wake seems to be emanating from the tail region, this disturbance propagates 2 or 3 chord lengths down the wake then rectifies itself. Apart from this one small blip the results are quite good and a vast improvement on the first new configuration.

7.3 CONFIGURATIONS AT 10° ANGLE OF ATTACK

Continuing the current trend of the analysis, the angle of attack is now increased to 10°.
The original UAV, fig. 32, yet again is providing the basis of the analysis and provides the expected patterns and wake quite well.
The higher angle of attack has resulted in the high pressure on the nose moving further down. The suction region on the upper surface of the wing has become very large and very negative as would be expected. However, there are unusually high pressures that can be seen at the very rear of the fuselage beyond the wing trailing edge, no explanation as to this occurrence can be offered.
The tail has the suction region on the horizontal tail upper surface and also low pressures on the leading edge tip that would intersect with the tailboom, further back along this edge is a region of high pressure.
The wake in fig. 33 is showing some signs of breakdown, the tip vortices are large and present, however showing signs of deterioration. The same can be said of the fuselage wake, which is large and irregular too.

In comparing the original UAV with the UAV with the change in aerofoil it can be seen that the results of this new design appear to be superior in some ways to those of the original. Though this in no way should be mistaken for saying the new design appears to be in it itself a better design.
The UAV MS 0313, fig. 34, has a very good pressure distribution, everything in the right place and no abnormalities. High pressure on the nose, suction pressure on the upper surface

of the wing, high pressure on the fuselage under the wing leading edge and the tail is the same as previously since it is modelled in an identical way.
The wake, fig. 35, is very good also. The tip vortices show good form, they are large but curl over nicely. The fuselage wake seems to remain very compact and not be disrupted and expand as in other cases.

Increasing the wingspan as in fig. 36 changes very little of the results of the previous case. Thus, everything is pretty much identical with the exception being that the suction region on the upper surface of the wing is larger, and most probably a drag penalty associated with it, but one disadvantage of this package is that this cannot be assessed.
The wake, fig. 37, appears almost identical to that seen in fig. 35 for the previous configuration.

The first new UAV configuration at 10^{o} angle of attack, visible in fig. 38 has completely broken down. Totally irregular pressure distributions that make no sense, the wings seem to have stopped generating lift, large areas of stagnant flow on the upper surface of the wings, the list goes on.
Examining the wake in fig. 39, it is clear there is no coherency about the wake, it is basically just a jumbled mess and in turn is reverting upon itself and affecting the flow over the UAV. The signs were there at 5^{o} angle of attack and from that point to this the results have deteriorated to such an extent that the current results are of no use and any further analysis futile.

The second new UAV configuration, fig. 40, is still providing some worthwhile results, though there are signs of the results at the tail coming unhinged. The results are typical of an aircraft at high angles of attack, the large suction region on top of the wing and the stagnation region on the tip of the nose. There does however appear to be a region across the top of the fuselage where there is low pressures which cannot be explained. Vortex shedding is present at the rear of the fuselage, emanating form the intersection on the wings between the two profiles.
The wake, fig. 41, is showing slight signs of breaking up, hence the results at the tail. Though overall it does appear to be holding up to an extent and the tip vortices are quite well defined.

7.4 CONFIGURATIONS AT -5° ANGLE OF ATTACK

Turning now to the negative angles of attack, and firstly the original UAV, fig. 42, we see that the pattern over the aircraft is quite uniform. In this case the suction regions have transgressed to the underside of the lifting surfaces as can be seen by evidence of the effect on the adjoining bodies/aerofoils. Prevalent over the surface are the blue regions that denote the stagnation regions, primarily associated with points of contact with the oncoming flow and points of separation. Which are dictated by the modelling.
The wake associated with this case, fig. 43, remains fairly flat and uneventful, the fuselage produces a small wake whilst there is no evidence of tip vortices whatsoever.

The subsequent configurations of UAV – figs. 44 and 46 with the applicable wakes in figs. 45 and 47, primarily based around the original, all provide results of a similar nature to those described above. Despite large discrepancies at other angles of attack they seem to have been ironed out or eradicated as the attitude becomes more negative. Not very much can be learnt from these plots, they only really serve to provide numbers and values for use in plotting graphs later on.

Moving on to the new configurations provide differing results as would be expected.
In keeping with the previous trend it would appear that once again the new configurations have thrown up some strange results. Fig. 48 shows the first configuration with fig. 49 being the associated wake. Forward of the wing trailing edge everything appears to be as expected, though again the tail region looks somewhat abnormal with a unusually high regions of low pressure. This indicates that the flow is stagnating to a certain extent, though nothing on the aircraft surface would appear to be causing the flow to decelerate in any way.
Turning to the wake we see that the flow emanating for the fuselage seems to be unusually turbulent and not similar to those of the original UAV's wakes in the least. This once again can only be attributed to the limitations of the program or the incorrect meshing of the wake, which it has been seen can prove fundamental in producing good results.
The second new configuration, fig. 50, however, does look slightly more conventional and produce results that may well be expected., Possibly the only cause for comment being the tail region again which can be said to have abnormally low pressures when there should not be considering that the tail in this case is an aerofoil section, so it would be expected to see maybe a suction region, or at least slightly negative portion to the tail section.
The wake on the other hand, fig. 51, looks remarkably normal. It has been the case that abnormal pressure results have been supported by the presence of an abnormal wake, this does not appear to be the case in this situation.

7.5 DRAG POLARS AND LIFT CURVES

The object of the whole analysis process was to discover the effectiveness of the various designs. From the CFD analysis various values were obtained, the remainder were obtained via hand methods. For one reason or another some of the configurations did not seem to perform well using this analysis package, so the results gained from their analysis were neglected though noted.

Focusing on the drag polar firstly, fig. 52, it is clearly visible that the curves are all quantitatively similar, following the same shape and crossing value of the lift coefficient axis. The graph itself was produced at ARTI in Prague, Czech Republic, and mereni simply means experimental[5]. Being over precise with the results it could be said that the UAV MS 0313 with the increased span had the lowest zero lift drag value, though the margin by which it is the best is minutely small. Deviating away from this value, the CFD results can be clearly seen as they gradually digress from the experimental curve. This can be attributed to the lack of stall prediction and separation in the analysis. The increased span configuration shows the greatest deviation whilst the original UAV and that with solely the new aerofoil follow virtually the same curve.
In summarising, the results of the drag polars would prove to be inconclusive, as they do not highlight any major differences between the configurations. In fact, performance wise they would appear to be on an even par.

Next, turning to the lift curve slopes in fig. 53. It can be seen once again the curves follow virtually the same trend as each other and the experimental value, up to values where stall and separation cannot be accurately modelled by the program. The lines achieved form the CFD results are effectively straight lines running parallel to the experimental curves straight region. The original UAV appears to overpredict the lift, as would be expected with CFD, with only a minor discrepancy in the results at approximately 2^{o}. Apart from this the results are good. Changing the original UAV by adding the new profile sees the curve shift upwards, effectively suggesting that this new aerofoil generates more lift. Not forgetting the drag polars

this would suggest that lift as increased though no overall drag penalty can be seen, which is an ideal situation to be in.
Furthermore, increasing the wingspan again results in the curve shifting upwards, again without incurring any sort of appreciable drag penalty.
Lastly, it can be said that the curves were overly straight, though the important part of the graphs can be considered and those where it is felt are unnecessary, such as those beyond stall can be guessed at or neglected. Since the aircraft will not be expected to fly over the entire range of the curves, just a restricted region.

8. CONCLUSIONS

A number of points at this stage can be raised from the analysis. Firstly, the program on which the analysis was performed is worth a mention. The analysis was performed and the project fulfilled to a degree, however, the limitations of the program in turn limited the effectiveness of the analysis.
Primarily, the program is intended for design purposes with particular relevance to streamlined bodies, with the emphasis on aircraft and boats. Consequently, the meshing functions are not comprehensive enough to perform a full scale analysis of the configurations, which led to small changes in the UAV designs and a compromise in order to accommodate the shortcomings of the program. Meshing of the bodies in itself was not problematic, the majority of problems arose as a result of the wake meshing. The wake is meshed in a rather complicated way, whereby all lifting surfaces require a wake, which allows separation and the calculation of lift. A wake separation line must be defined along a mesh line, for instance on the trailing edge of the lifting surface. This line was limited by the fact it could not cross with any other wake separation line or wake, so this led to further small changes and compromises. It was possible for the wake to modelled using only 2 lines of code, though the method needed to do such a thing was another matter, and proved quite time consuming to understand and difficult to implement compared to the relatively straightforward process of modelling the body.
Furthermore, the program seemed to greatly dislike unconventional aircraft configurations. Whilst undertaking the modelling, several bugs were found and highlighted to the programmers, these remedied some of the problems though the overall process was still problematic. The UAV designs being analysed were fairly typical UAV designs though still unconventional. The tailbooms in the design proved too much, as parallel surfaces to the flow are not allowed, as they have no area perpendicular to the flow. Hence, tapering of portions of the aircraft was required. Unfortunately no amount of tapering could rectify the tailboom problem and these were subsequently removed from the model and all ensuing models. The design which had no tailbooms was not exempt form problems, the vee tail in this design also threw up strange results and seemed to have a very unstable wake.
A point of note here, in no way is the program used being criticised, it is merely being highlighted here that it was unsuitable for the purposes of this project and ideally some other program should possibly have been used.

Once the initial problems were overcome some worthwhile results were obtained. The initial idea was to analyse 5 designs, though in reality with all the problems only 3 could be compared with any real substance. The existing UAV was modelled as the benchmark, or control, though there were clearly visible instabilities in the wake when compared with other configurations, hence, most of the new designs seemed to fair well against the original. Thw newer configurations did give some results, though seeing as these deisngs seemed to drift away from the conventional model laid out by the program instabilities in the wakes were ever present. From this it was determined that the wake was a primary factor in the probe for good results. However, as mentoined above, modelling the wake was a rather problematic affair at times and allowed little room for variation, so if a wake was inherently bad then the resutls gained had to be accepted. Since the same process was adopted for modelling the wakes throughout all the configurations no remedy or possible rememdy can be suggested to improve the bad wakes and ultimately results..

The analysis was completed and all the configurations evaluated. The best performing aircraft was found to be the UAV design with the new aerofoil and increased span, simply because it

seemed to generate extra lift without any visible drag penalty. The new configurations threw up some interesting designs and it would be worthwhile to ananlyse these more thoroughly, with a proper analysis package that would show how they would perform as the results form this analysis proved to be quite inconclusive.

9. REFERENCES

1. Kuzdas, J., Smrcek, L. & Taylor, M. N., Development of a SOJKA Remote Pilot Vehicle System, International Conference on RPV, Bristol, UK, 1994, ISBN 086 292 014

2. LOFTSMAN Version 4.3 Instruction Manual, Documentation Copyright Peter Garrison 1989-2000

3. DIGITAL WIND TUNNEL / CMARC Instruction Manual, Documentation Copyright Aerologic 1995-2000

4. POSTMARC Version 3.7 Instruction Manual, Documentation Copyright David Pinella 1995-2000

5. Bornhorst, E. & Mala, J., Aerodynamicke Charakteristicky Modelu Terce – Sojka III (Aerodynamic Characteristics of the Sojka III Model), ARTI Report P65/2110/91, 1991

10. APPENDIX A

UAV CONFIGURATION WITHOUT TAILBOOMS

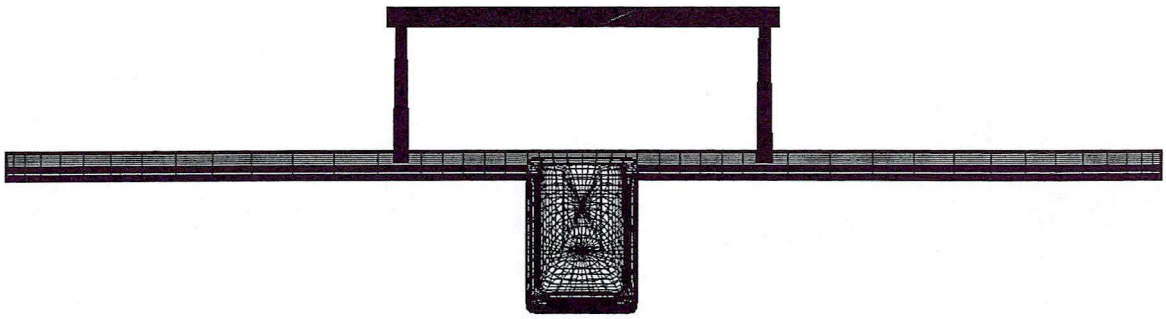

Front elevation of UAV without tailbooms

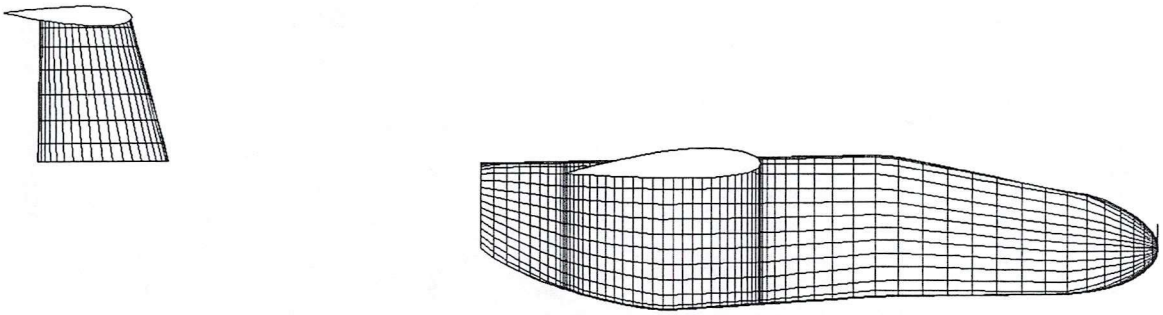

Side elevation of UAV without tailbooms

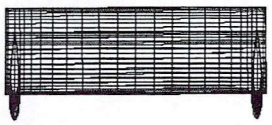

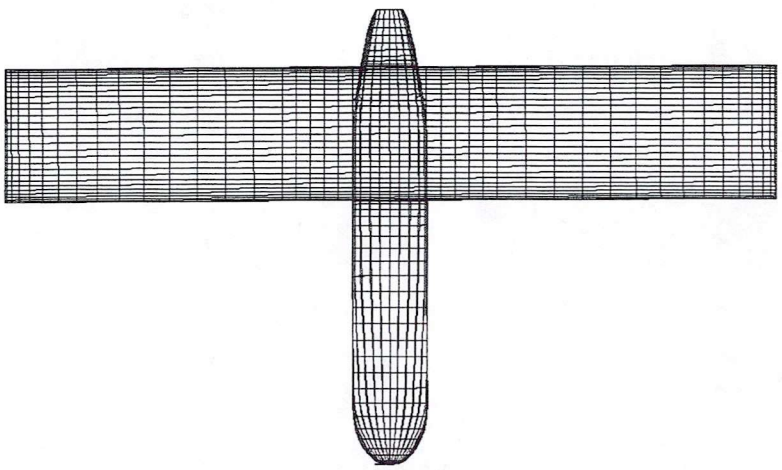

Plan elevation of UAV without tailbooms

UAV CONFIGURATION WITH MS 0313 WING PROFILE

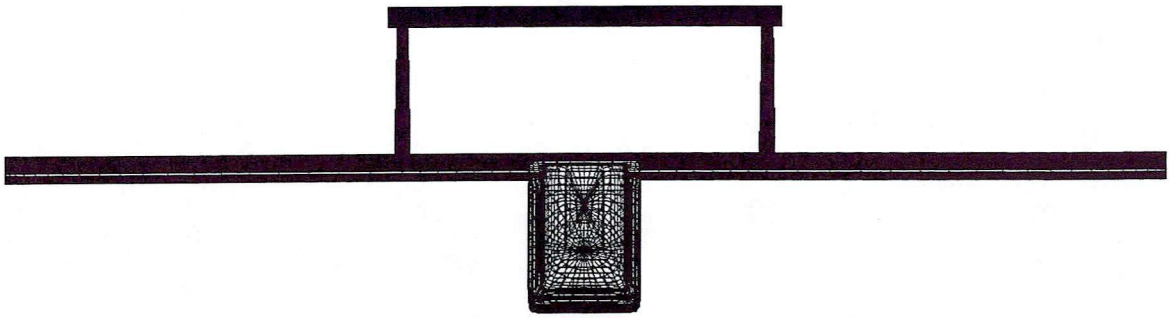

Front view of UAV MS 0313

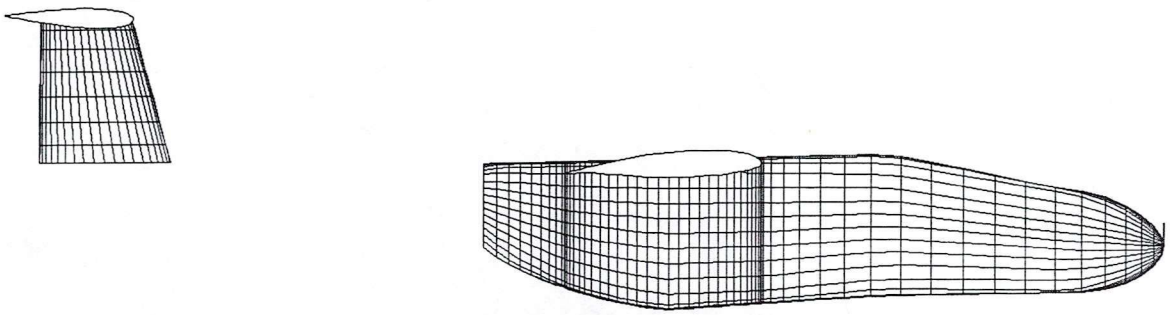

Side view of UAV MS 0313

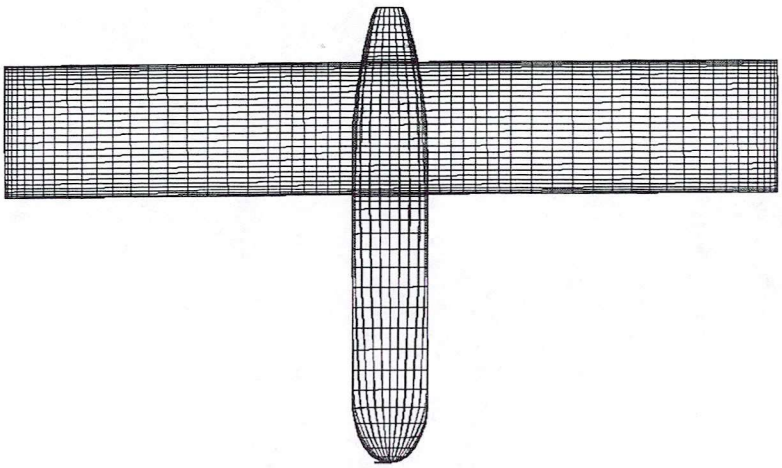

Plan view of UAV MS 0313

UAV CONFIGURATION WITH MS 0313 PROFILE AND INCREASED SPAN

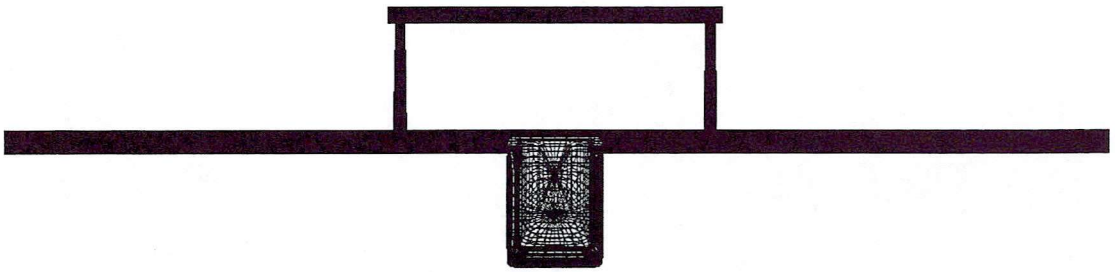

Front view of UAV MS 0313 with increased span

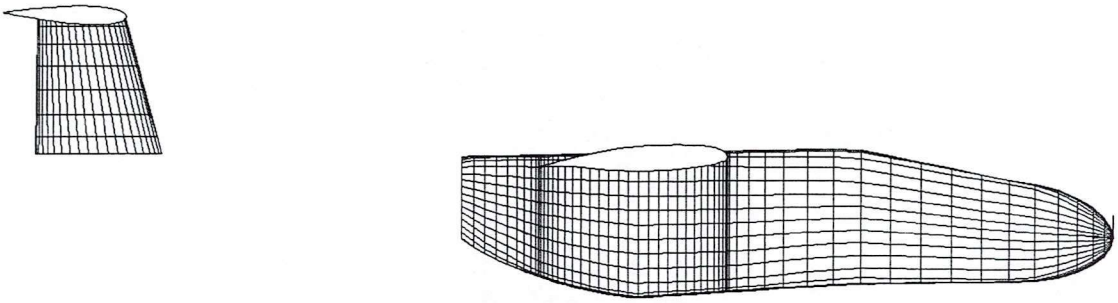

Side view of UAV MS 0313 with increased span

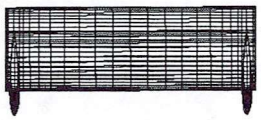

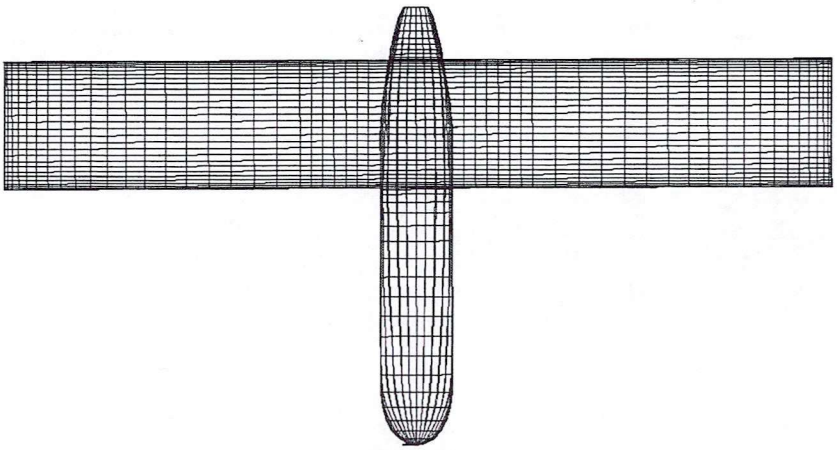

Plan view of UAV MS 0313 with increased span

NEW UAV CONFIGURATION 1

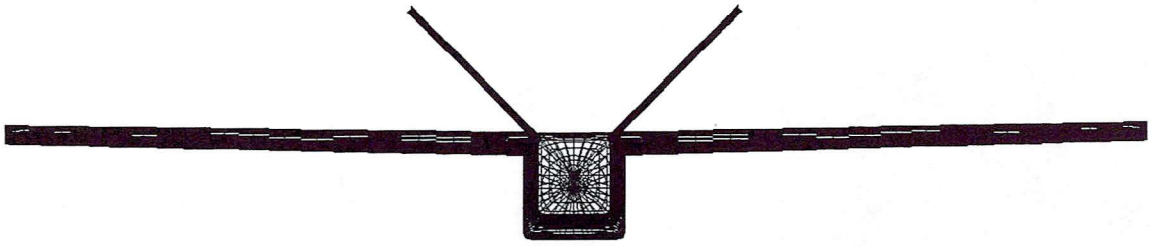

Front view of new UAV configuration 1

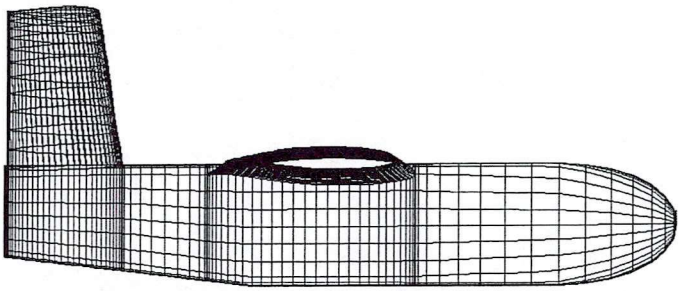

Side view of new UAV configuration 1

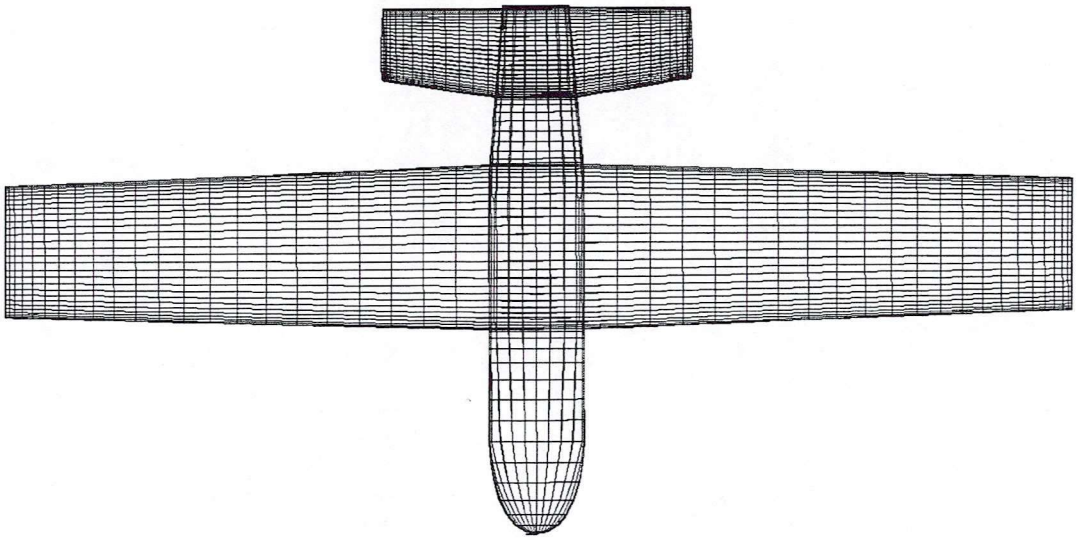

Plan view of new UAV configuration 1

NEW UAV CONFIGURATION 2

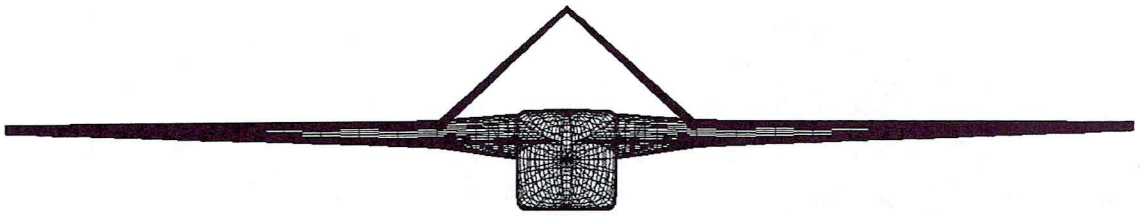

Front view of new UAV configuration 2

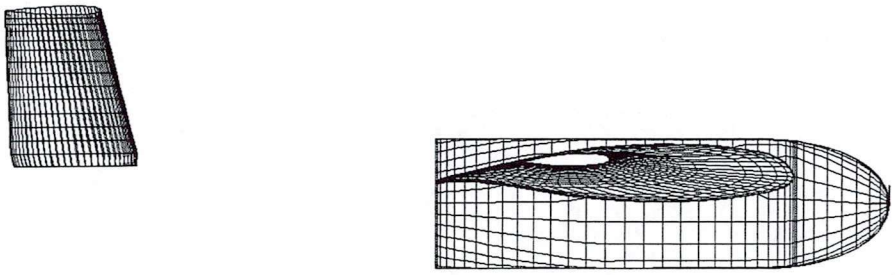

Side view of new UAV configuration 2

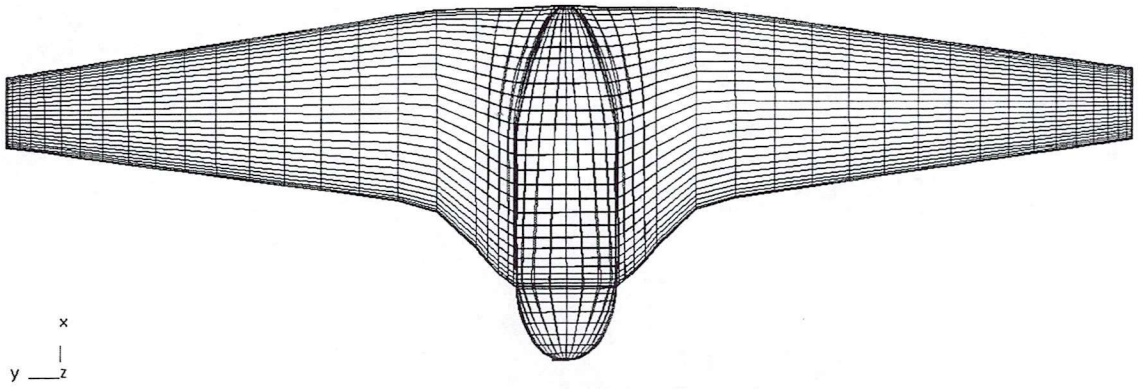

Plan view of new UAV configuration 2